YEDITEPE SPINE MESH: MODELING AND VALIDATION OF A PARAMETRIC FINITE ELEMENT MODEL OF THE LUMBAR SPINE

by
Oğulcan Güldeniz

Submitted to Graduate School of Natural and Applied Sciences
in Partial Fulfillment of the Requirements
for the Degree of Master of Science in
Mechanical Engineering

Yeditepe University
2020

YEDITEPE SPINE MESH: MODELING AND VALIDATION OF A PARAMETRIC
FINITE ELEMENT MODEL OF THE LUMBAR SPINE

APPROVED BY:

Asst. Prof. Dr. Ali Fethi OKYAR ……………………………
(Thesis Supervisor)
(Yeditepe University)

Asst. Prof. Dr. Andaç HAMAMCI ……………………………
(Yeditepe University)

Asst. Prof. Dr. Süleyman Serdar YÖRÜK ……………………………
(Beykent University)

DATE OF APPROVAL: …./…./2020

ACKNOWLEDGMENTS

It is with immense gratitude that I acknowledge the support and help of my supervisor Dr. Ali Fethi Okyar. Pursuing my thesis under his supervision has been an experience. Without his assistance, guidance, and dedicated involvement in every step throughout the process, this thesis would have never been accomplished. I would very much like to thank him for his support and understanding over these past seven years.

I also take this opportunity to express my gratitude to all of the department faculty members, BIAS Engineering, and my dearest friends for their help and support.

ABSTRACT

YEDITEPE SPINE MESH: MODELING AND VALIDATION OF A PARAMETRIC FINITE ELEMENT MODEL OF THE LUMBAR SPINE

Finite element analysis is a powerful tool that is often used in order to study the biomechanical response of the lumbar spine. Anatomical meshes that are used for such analysis are often fixed, hence preventing the tuning of morphometrical parameters. The primary objective of this study was to develop a segmented finite element model and a parametric finite element model that would allow the independent tuning of previously determined morphometrical parameters of the L4 L5 spinal level. An extensive verification procedure was applied via convergence studies. As our validation metrics, moment-rotation curves, intradiscal nuclear pressures, and facet joint contact forces were collected from these both models, as well as the data from the literature, and compared with each other in order to validate our models. Segmented finite element model was observed to be in a good agreement with the literature, therefore, validated for all of our validation metric predictions. The parametric finite element model, on the other hand, was observed to be in a good agreement with the segmented finite element model, and with the literature, for its moment-rotation curve predictions and intradiscal nuclear pressure predictions. Facet joint contact forces were observed to be overpredicted by the parametric finite element model. Future study on the facet joint geometry and inclusion of the non-symmetric nature of the vertebrae geometry was proposed as a future study.

ÖZET

YEDİTEPE OMURGA AĞI: LOMBER OMURGANIN PARAMETRİK SONLU ELEMANLAR MODELİNİN MODELLENMESİ VE GEÇERLİLİĞİ

Sonlu elemanlar analizi, lomber omurganın biyomekanik tepkisini incelemek için sıklıkla kullanılan güçlü bir araçtır. Bu analiz için kullanılan anatomik ağlar genellikle sabittir, böylece morfometrik parametrelerin ayarlanmasını önler. Bu çalışmanın temel amacı, önceden belirlenmiş L4 L5 omurga seviyesinin morfometrik parametrelerinin bağımsız olarak ayarlanmasına izin verecek şekilde segmentli bir sonlu eleman modeli ve parametrik bir sonlu eleman modeli geliştirmektir. Yakınsama çalışmaları ile kapsamlı bir doğrulama prosedürü uygulandı. Doğrulama ölçütlerimiz olarak, moment-dönüş eğrileri, intradiskal nükleer basınçlar ve faset eklem temas kuvvetleri bu iki modelden ve literatürden elde edilen verilerden toplanmış ve modellerimizi doğrulamak için birbirleriyle karşılaştırılmıştır. Segmentli sonlu elemanlar modelinin literatürle iyi bir uyum içinde olduğu gözlendi, bu nedenle, ölçüm karşılaştırmalarımıza göre sonuçları geçerli kabul edildi. Parametrik sonlu elemanlar modelinin, ani dönme eğrisi tahminleri ve intradiskal nükleer basınç tahminleri için segmentli sonlu elemanlar modeli ve literatür ile iyi bir uyum içinde olduğu görülmüştür. Faset eklem temas kuvvetlerinin parametrik sonlu elemanlar modeli tarafından fazla tahmin edildiği gözlenmiştir. Faset eklem geometrisi ve omur geometrisinin simetrik olmayan doğasının dahil edilmesi üzerine gelecekte bir çalışma yapılması önerilmiştir.

TABLE OF CONTENTS

LIST OF FIGURES

LIST OF TABLES

LIST OF SYMBOLS/ABBREVIATIONS

U	Strain energy density function
C_{10}	Shear modulus
$k1$	Fiber stiffness coefficient
$k2$	Fiber nonlinearity coefficient
κ	Fiber dispersion parameter
$\bar{I}_1$	Volume preserving part of the first invariant of the right or left Cauchy-Green deformation tensor
$\bar{I}_4^{ii}$	Volume-preserving part of two pseudo invariants measuring strain in the fiber directions
$\bar{E}_i$	Lagrange strain component through fiber direction
RE	Relative error
D	Collected data
σ_r	Radial cauchy stress

LBP	Low back pain
IDP	Intradiscal nuclear pressure
FJF	Facet joint contact force
CAD	Computer-aided design
FE	Finite element
IVD	Intervertebral disc
NP	Nucleus pulposus
AF	Annulus fibrosus
STL	Stereolithography
ALL	Anterior longitudinal ligament
PLL	Posterior longitudinal ligament
SSP	Supraspinous ligament
ISL	Interspinous ligament
ITL	Intertransverse ligament
FCL	Facet capsular ligament
LFL	Ligamentum flavum

V&V	Verification and validation
RBE2	Rigid body elements in Marc Mentat 2019
L	Left lateral side
R	Right lateral side
S	Symmetry condition between left and right lateral side

1. INTRODUCTION

One of the main musculoskeletal disorders that cause disability effects on the patient is low back pain (LBP) [1]. LBP is also known to be one of the first reasons that limit the activity of the patient, which may cause sick leave, and maybe even hospitalization [2]. More than 50 percent of adults are known to be experiencing LBP [3, 4]. Sagittal curvature of the spine has been reported to be one of the factors that is directly related to the degenerative change[5], which reported to be associated with the LBP cases [6–8]. Similarly, mechanical loads are also reported as one of the most important factors that are known to be a factor related to LBP [9]. Degenerative lumbar disc disease has also been reported as a factor that causes LBP [10]. Furthermore, spinal fusion appears at the top of the list of surgical interventions that are most commonly performed [11]. Like many other musculoskeletal disorders, spinal fusion is also studied to be related to the loss of mobility at the spinal level where the disorder is located and observed to be directly correlated with the increased stress loadings on the other spinal levels [12, 13]. With such an influence of the mechanical loadings on the musculoskeletal disorders of the lumbar spine, determining the mechanical response of the lumbar spine in terms of load-sharings and kinematics under various mechanical factors such as spinal curvature becomes essential [14]. Moreover, such high demand and requirement to the spinal intervention would put research on the mechanical response at the scope of many researchers, to improve the current methods, currently used medical devices, and increasing the success rates of such spinal interventions.

In terms of regulatory requirements of the medical product design, a review of each design step is required, which increases the costs of the design process with every additional step, and requires a lot of time [15, 16]. Even though current technologies have been improving the rapid prototyping and reviewing of these design steps, understanding the interaction of the designed medical product with the related tissue is still a necessary step to achieve a complete evaluation of the designed product [17]. Experimental studies are providing direct results; however, conducting such experiments are expensive and time-consuming [18]. In that sense, finite element (FE), and musculoskeletal models are widely used to speed up the design steps, and assessing the interaction between the designed product and the related tissue [19–21].

FE and musculoskeletal models of the lumbar spine to *in silico* collect some necessary data needed for various purposes and assess the performance of the medical products has been an appealing alternative to the experimental approach [22–26]. While both approaches are performed to evaluate same data, *in silico* approaches such as FE method provides accessibility to measurements such as intradiscal nuclear pressure (IDP), facet joint contact force (FJF), bone strain, and the annulus fibrosus strain that can not be easily collected via experimental studies [18]. In literature, it is possible to find many previous research that has been performed to understand the mechanical response of the lumbar spine [21, 27–30]. It is important to note that many of those computational research are conducted either by using FE models or by musculoskeletal models as preferred options. Extensive material property studies of the spinal tissues are well reported in the literature, which can directly be implemented to the FE models [31]. Bone tissues are usually represented by using linear elastic material properties since expected strain results are relatively infinitesimal [32]. An extensive summary of the most known eight FE models of the lumbar spine that includes almost all the necessary details to develop such models were provided in the comparison study of Dreischarf et al. [31].

Modeling the geometry of the spinal segments is essential for the prediction capability of the models since geometrical complexity is reported to be quite related to the accuracy of the results [33]. FE models of the spine in the literature are generally subject-specific models that accurately represent patient-specific geometry [34, 35], or models generated as the average of a population of models that lacks to represent patient-specific features [36–39]. Models based on patient-specific geometries represented the patient geometry precisely [17] and suggested to be more reliable since such an approach would eliminate the oversimplification of the problem [40, 41]. Moreover, studying more than one patient-specific model would improve the understanding of researchers by adding statistical power to the study [42]. However, resulting models are fixed, which means that the whole process of developing the model is required to be repeated for every single patient [43]. Therefore, generating such patient-specific models lack robustness, which increases the time spend, and the cost [44].

In 1991, to the authors' knowledge, Breau et al. [45] developed the first human ligamentous lumbar spine FE model by using computed tomography (CT) scans. In that study, they defined vertebrae as two solid bodies (vertebral body and posterior bony section) connected to each other by rigid elements, and they only focused on the soft tissue. Later on, in 2007, a patient-specific FE model of the thoracolumbar spine was developed by Tyndyk et al. [46]. They represented the patient-specific geometry by using various methods very well. Ayturk et al. [30] performed an extensive study to develop a patient-specific FE model of the lumbar spine in 2011. They used patient CT scans to build the patient-specific model. He has stated the importance of the usage of patient-specific models to the model predictions and further evaluated his model by performing a mesh convergence test to validate his results. He also has stated the fact that verification & validation studies were not that common for the FE models of the lumbar spine. Later on in 2013, Park et al. [47] also prepared a patient-specific FE model of the lumbar spine by using CT scans. They captured the geometry quite accurately. In 2016, Naserkhaki et al. [14] studied the effects of variations on the spinal curvature. They reported that spinal curvature caused significant changes in the results, such as range-of-motion, intradiscal nuclear pressures, and facet joint contact forces. Therefore, it explained the importance of using patient-specific models for further research. All the models mentioned in this paragraph are developed by using CT scans of a single patient, therefore patient-specific in nature. Many of them did not perform a mesh convergence study to validate the accuracy of their model mesh. Furthermore, many of the models lack the statistical data needed to validate the results of the research further. It is presumed that the intensive process of developing patient-specific data for a large population was avoided because of the inefficiency of the rigorous and time-consuming steps to be followed to develop such models.

Lavaste et al. [39] parametrically modeled the geometry of the vertebrae by using only six parameters and generated a model representing the lumbar spine. Their model was symmetric in nature. To our knowledge, it was the first study that presented a fully-parametric model that was allowing independent tuning of its morphometric parameters. They validated their model in terms of global coherence. As a result, they tuned their model with patient-specific parameters and presented the results accordingly. The earliest model to our knowledge that was started to be tuned with different morphometrical parameters was proposed by Smit et al. [48]. In later studies, that model was tuned with the mean parameters of a population to represent the mean geometrical shape was presented by Zander et al. [24]. Their model was also symmetric in nature. The same model was also used in a later study by Wilke et al. [49] in 2005. They compared their computational results with an experimental study performed previously. However, they did not mention whether they performed that computational study by tuning their model with the specimen's morphometrical parameters or not.

A further parametrical FE model of the lumbar spine was proposed by Ezquerro et al. [50]. Their parametrical vertebrae models were allowing the tuning of up to 55 parameters. However, even though such a parametrical model would allow them to work on subject-specific models, they choose to generate their model with mean parameters collected from the literature. In 2008, Little et al. [51] proposed a slightly different approach. They landmarked some points on the CT scan, which they extracted coordinates, and then they used a python script to automatically generate the geometry of the patient-specific model. However, even though how much this approach sounds so robust, it was not capable of representing the vertebrae geometry altogether. Therefore, they used rigid body elements to generate the posterior bony section, where the ligaments are attached. Their approach provided reliable results. However, since the posterior bony section rigidly modeled, it lacked to accurately represent the information that might be collected from the bony tissue.

In an earlier attempt, in 2008, Naddeo et al. [52], and Nicola et al. [38] studied on further parameterizing the lumbar spine. They stated the importance of parametric models of the spine by saying that parametric models combined the accuracy of volumetric rendering and pragmatism and speed of simplistic models. Similar to previous studies mentioned, they developed symmetric models. However, they lacked to validate their model against subject-specific data. Later on, a relatively significant increase was observed on the amount of intensive research that has been performed to speed up the patient-specific model development process by using parametric models. Campbell et al. [53] developed a method to automatically generate patient-specific FE meshes of the lumbar spine. They used the landmarking method to update their mesh with data from a patient. They were also the first ones to our knowledge to build up such a statistical parametric model, and to perform an extensive mesh convergence study and validation. They validated their model by comparing it with manually generated patient-specific models from a CT scan and further validated it by comparing it with the literature. Their research could be considered successful in many aspects. In a later attempt, Lavecchia et al. [17] proposed a tool called "Lumbar Model Generator." By using this tool, they have managed to develop patient-specific FE models of the lumbar spine. In terms of using an approach to manipulate an existing mesh, this approach was also similar to what Campbell et al. [53] proposed. Both models proposed by Campbell et al. and Lavecchia et al. are observed to be symmetric about the sagittal plane, excluding the biomechanical disorders that can occur because of the non-symmetric nature of the spine. Even though examples of studies similar to theirs were easy to find in the literature, almost all of them generated parametric meshes. Current literature still lacks an extensively validated parametric computer-aided design (CAD) model of the lumbar spine.

Previously, we have proposed a parametric CAD model of the lumbar spine, including the intervertebral discs[44]. That model was developed by considering the spine morphology as it is described in the literature and was designed accordingly, including the morphometrical parameters[54]. The generation process of that model was described with a three-layered holistic approach and further explained thoroughly with a generation algorithm. In order to add the statistical power to our study, that model was further generated with morphometric parameter measurements collected from seven patient's CT scans, and each model was compared in terms of Hausdorff distance with the segmented stereolithography (STL) model generated from the same patient's CT scan. Statistical analysis showed a good geometrical correlation between the CAD model and CT scan for all subjects. Therefore, we validated our model in terms of geometrical correlation with segmented CT models.

However, further work was necessary in order to validate the mechanical response of our model too. In this study, we primarily focused on this aspect. For a single patient, we developed two FE models: segmented and parametric. The segmented FE model was developed properly as described in the literature, while the parametric FE model was developed using a novel approach. Both of these model were subjected to 10 Nm pure-moment in order to simulate the flexion, extension, lateral bending, and axial rotation motions. An extensive mesh convergence test was performed to understand the accuracy of the predictions. In order to validate them, moment-rotation curves, IDPs , and FJFs were collected and compared with each other, as well as with the literature.

1.1. MORPHOLOGY OF THE LUMBAR SPINE

Morphology of the lumbar spine was divided into three main sections: vertebra, intervertebral disc, and ligaments. Morphology of these sections was explained in detail, and the FE modeling approaches from the literature to model them were summarized.

1.1.1. Vertebrae

In the literature, vertebrae were generally described with two sections: vertebral body and posterior bony section. Vertebral body was also divided into two sections: cortical and cancellous bone. The reason behind that division is the difference in the material properties of these regions. Even though material properties do not differ much from each other: cortical bone is described as the most stiffer section, while cancellous bone is the least stiffer section of the vertebrae [31]. In Figure 1.1, sections of the vertebrae are illustrated.

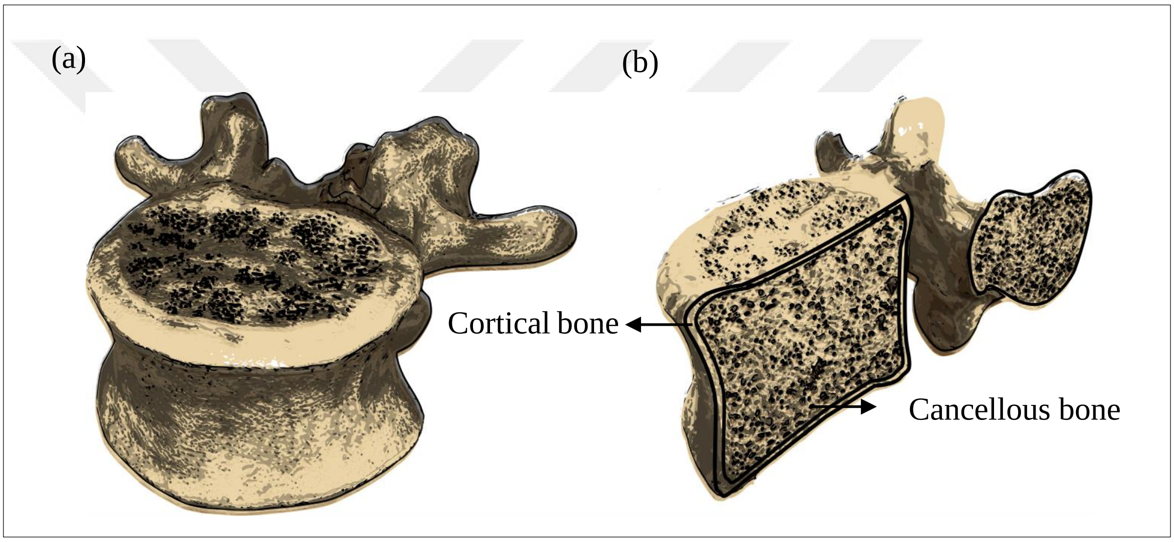

Figure 1.1. (a) Lumbar vertebrae, and (b) right lateral cross-section of it.

In the FE method, this tissue is generally modeled with linearly elastic and isotropic material definitions [47]. However, there are examples in the literature that also modeled this tissue with linearly elastic and transversely anisotropic materials [30, 55].

1.1.2. Intervertebral Disc

Intervertebral disc (IVD) consists of two distinct sections: the nucleus pulposus (NP) that covers the inner region, and the annulus fibrosus (AF) that covers the outer region of the intervertebral disc. The nucleus pulposus in the center of the intervertebral disc possesses a more gelatinous structure, while the annulus fibrosus that surrounds the nucleus pulposis possesses a more collagenous structure. The annulus fibrosus also possesses concentric lamellae tissue that consists of collagen fiber tissue and non-fibrous matrix (water, proteoglycans, and noncollagenous proteins) surrounding the intervertebral disc and the nucleus pulposis, and reaches into the spinal ligaments covering the tissue [56]. These fibers provide tensile properties to the IVD [57]. Collagen fibers of the AF are reported to be oriented with approximately 30 and 150 degrees, referred to as the transverse plane of the spine. However, the orientation angle of the collagen fibers is also reported to be varying in circumferential and radial directions [58]. IVD contains mostly water in its structure (65-90 percent), collagen (15-65 percent dry weight), proteoglycans (10-60 percent dry weight), and other proteins (15-45 percent dry weight) [59]. In Figure 1.2, sections of the intervertebral disc are illustrated.

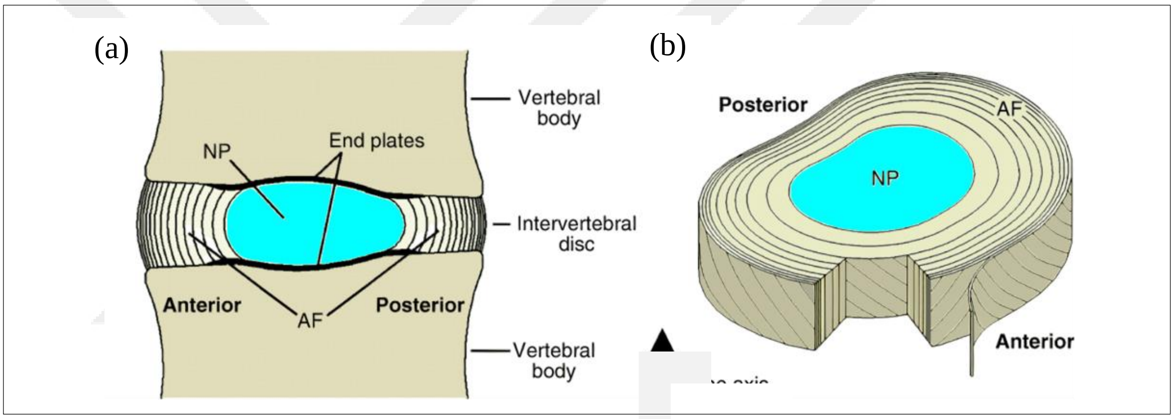

Figure 1.2. (a) Right-lateral cross-section of the intervertebral disc and (b) intervertebral disc (60).

For FE modeling of the NP, most of the previous research proposed to model that tissue as modeling it with incompressible fluid elements [47, 51]. However, since many FE modeling tools do not allow fluid element definition, others modeled the same tissue as a linearly elastic and isotropic model with Poisson's ratio close to 0.5 as much as possible to implement the incompressibility effect, therefore maintaining a fluid-like behavior [30].

Despite the FE modeling of the NP, there are many different approaches towards modeling the AF collagen fibers, which has evolved a lot with the time passing. In 1994, Shirazi-Adl et al. [60] modeled their AF fibers of their FE model of the lumbar spine with membranes varying the thickness of the fibers dependent on the depth. They assigned non-linear material properties to these membranes in order to increase physiological accuracy. A similar approach was also observed in the studies of Breau et al. in 1991 [45], and Park et al. [47]. However, that approach was impractical, since each fiber was supposed to be assigned individually. Later on, a continuum element approach was adopted by researchers. With this approach, the material formulation was representing a phenomenological constitutive model of fibers and the bulk material that does not represent individual fibers and does not indicate the number of fibers. Therefore, that was saving the researchers from the time spend to assign each fiber individually. Continuum approach was used in the studies of Ayturk et al. [30] in 2011. As the continuum model, they used hyperelastic anisotropic Yeoh material properties. The advantages that continuum models provided made it the preferred option for the modeling of AF media, and its' usage over time has increased. In 2016, Campbell et al. [53], used a different continuum material formulation called Holzapfel-Gasser-Ogden model to define the AF mechanical properties. The same model was later on used in the studies of Coombs et al. [18] with the mean material properties collected for the same material model.

1.1.3. Ligaments

Seven different ligamentous tissues cover the entire lumbar spine and add stiffness against all degree-of freedoms. These ligaments are anterior longitudinal ligament (ALL), posterior longitudinal ligament (PLL), supraspinous ligament (SSP), interspinous ligament (ISL), intertransverse ligament (ITL), facet capsular ligament (FCL) and ligamentum flavum (LFL). It has been reported that ligaments consist of collagen fiber tissue and non-fibrous matrix, which is similar to AF tissue. Tensional loading on the ligamentous tissue causes an uncoil in the collagen fibers, which causes the fibers to align along the axis of the load, and that causes the tissue to show its maximum stiffness. However, that only happens under tension; similar behavior has not been reported under compressional loadings. In other words, ligaments behave like a non-linear spring under tension but remain passive under compression. Therefore, fiber length, orientation, and stiffness values are reported to be essential variables in the construction of lumbar spine models [61]. In Figure 1.3, ligaments of the lumbar spine are illustrated.

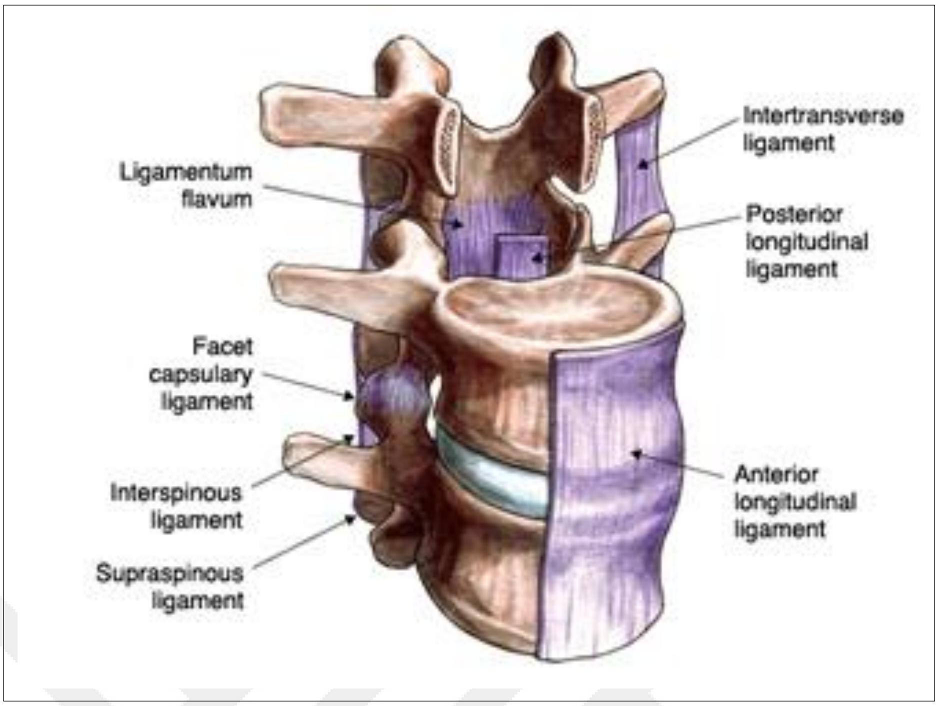

Figure 1.3. Ligaments of the lumbar spine [62].

In FE modeling, there were various approaches towards modeling of the ligamentous tissue. In general, spring-like behavior of the ligaments was implemented to the models by using 1-dimensional spring elements that respond to tension load only but remain passive under compression load. In 2006, Rohlmann et al. [63] implemented the behavior of the ligaments by defining exponential force-displacement curves in order to capture the non-linear behavior under tension. That approach with the proposed exponential fits was used by some other researchers too [30]. In a later study, in 2017, Coombs et al. [18] defined the spring-like behavior of the ligaments by using mean stiffness values for tension. Even though this approach was more simplistic than the others, they captured a good fitting relation with their experimental and FE results. There are also models that were modeled the ligaments by using truss elements [47].

1.2. VERIFICATION AND VALIDATION

Accurate and quantitative computational modeling of any biomechanical tissue has the potential to represent the reality up to a certain level. Such computational models have the capability of estimating valuable mechanical data, which becomes more critical when the location of interest is hard to reach, or out of reach with the current experimental methods. Furthermore, the non-invasive nature of the computational models also increases its value [64]. The current increase in computational power due to the recent developments also renders researchers capable of preparing finely discretized models and increasing the detail of the output data. Such advancements of the computational modeling are making it a preferred option in the biomechanical research field [65]. However, the credibility of the model also needs to be assessed before relying on its predictions. In order to achieve such a goal, computational models must be verified and validated by accurately assessing the model predictions by using computational and experimental protocols, that inevitably establishes the evidence about the accuracy of the model predictions [30]. Verification and validation (V&V) are reported to be quite an essential part of any computational research [66]. In literature, it is possible to find much research stating the importance of V&V of the computational models [67–69]. Specifically, for the topic of this study, there is also much research performed V&V procedures for their computational spine models, and presented their findings [19, 20, 30, 31].

In summary, verification can be explained as the process of assessing the accuracy of whether a computational model implementation can represent the description and the solution of a specific case scenario, whereas validation can be explained as the process of comparing the resulting data of the computational model with experimental data. With a more straightforward explanation, verification is solving the equations right while validation is solving the right equations [70, 71].

In order to understand V&V, understanding the notion of error and accuracy is necessary. Error and accuracy have an inverse relationship between them. With broader terms, while error represents the difference between computational results and so-called true results, accuracy represents how close our results to the truth [72]. Types of error can be gathered under two groups for computational studies: numerical and modeling errors. Discretization error that is often observed in the FE method would be a good example of the numerical errors, which is often caused by dividing the problem into a number of discrete sub-problems that could not be sufficient to define the exact geometry [67–69]. Modeling errors often occur because of the wrong definition of the boundary conditions, load cases, and material properties of the models that do not represent the reality well. On the other hand, experimental studies have systematic errors, as well as random errors. So that notion of correctness is, in fact, impossible to reach. However, reaching absolute correctness is actually not necessary from an engineering perspective since the level of accuracy of any study ultimately depends on the aim of the study. Therefore, a statistically relevant comparison of any computational data with relatable experimental data by systematically stating the errors would be sufficient to assess the accuracy of any computational model [67, 69].

With a more general definition, verification has been described as the process of understanding how accurately a computational model represents the mathematical model and its solution. However, a successful verification process does not generally mean that the developed computational model would provide the same accuracy for other load cases and boundary conditions, but only verified for a set of benchmark problems [69]. The verification of computational models are generally divided into two: code verification and calculation verification [66]. The code verification process is generally already performed by the software companies whose products are on use to develop such models. Therefore, most of the research performed on computational model development by using such commercial software code verification is already completed [73, 74]. Calculation verification, on the other hand, is most necessary in order to understand whether the discretization level of the problem accurately represents the geometry. In order to complete that step, mesh convergence studies are performed. Therefore, the error caused by discretization is assessed systematically [73]. Generally, mesh convergence studies are performed by systematically refining the mesh density until a previously chosen output parameter converges to a certain level, or error decreases below the required accuracy [65, 75]. In order to separate the mathematical errors from validation, the verification process must always need to be done beforehand.

Validation is defined throughout the literature as the capability of the computational model to predict the reality, which is mostly done by comparing the prediction results with experimental data [66]. Such a comparison could also be made by using the experimental data from the literature. However, integrity between the computational model and the experiment must be ensured. Researchers need to prepare their computational model as close to the experimental setup as possible, and other specific details such as material properties or maybe even geometry must be accessible. Otherwise, any detail that was failed to be implemented to the computational model would create uncertainty. The experimental error must also be reported in the subjected experimental study [64]. Such experiments could also be performed with the purposes of validating the predictions of the computational model, where possible. That would inevitably increase the accountability of the computational model. However, performing such an experimental study is, in general, not possible for many [66]. Furthermore, a validation metric also needs to be chosen. Such a metric could be chosen accordingly to the intended output of the computational model [67]. Validation on one specific validation metric does not necessarily mean that other output data collected will be valid too, depending on the type of data, further validation could be necessary [64].

In the materials and methods section, the development process of both FE models, analysis setup and boundary conditions, mesh convergence test for verification, and validation process was explained in detail. In the results section, convergence test results, moment-rotation curves, IDPs, and FJFs for both model was provided, and a comparison made between them and the other models, as well as with the experimental data reported. In the discussion section, a further comment was made to the findings, and limitations of our study were elaborated. Finally, in the conclusion section, a summary of our findings and validation process was provided.

2. MATERIALS AND METHODS

For this study, two different functional single unit FE models of the L4 L5 vertebral level were developed. These models were referred to as segmented and parametric FE models. Both of the models developed by using the same patient’s CT scan data. Segmented CAD model vertebrae as developed by applying segmentation methods to the patient’s CT scan, and generating a solid model from that. For the parametric CAD model vertebra, we used a previously developed parametric CAD model of the lumbar column [44]. The parametric CAD model was regenerated by using the parameter measurements from the same patient’s CT scan. After the development of the CAD model of the segmented and parametric vertebra, the intervertebral disc was modeled in between the vertebrae for both. After that, all the models meshed accordingly in order to obtain the FE models. Lastly, Lumbar vertebral ligaments were adequately included in the FE models. After the development of the FE models, both of them were subjected to the same loading conditions under the same boundary conditions in order to simulate main motions: flexion, extension, lateral bending, and axial rotation. An extensive verification process was performed by mesh convergence study. The results of both FE models were compared with each other, as well as with the literature in order to validate them. MSC Apex Jaguar was used for the meshing of the models, while simulations were performed on Marc Mentat 2019. In the following sections development of the segmented and parametric FE models and their validation steps will further be elaborated.

2.1. DEVELOPMENT OF VERTEBRAE FE MODELS

2.1.1. Development of Segmented FE Model Vertebrae

The segmentation model of the patient’s CT scan was developed by using an open-source software named 3DSlicer [76, 77]. An STL model [78] of the lumbar vertebrae was developed via 3DSlicer by segmenting the high-intensity voxels of the CT scan representing the bone tissue.

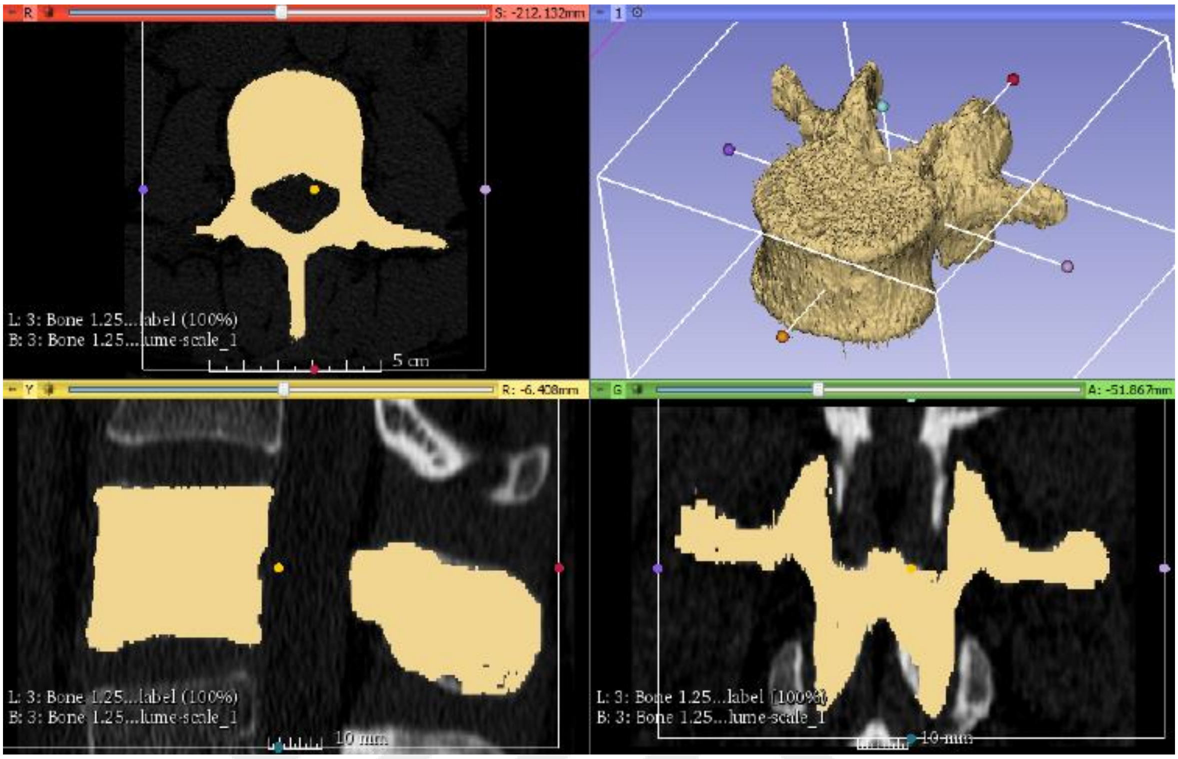

Figure 2.1. Superior, posterior, and right view of sample vertebrae from 3Dslicer during the segmentation process.

The resulting STL model was then imported to Autodesk Meshmixer version 3.5.474 in order to edit it and prepare for the FE model generation. Other vertebral segments were deleted since, in this study, we only focused on the L4 L5 spinal level. Figure 2.2 illustrates the STL model of L4 and L5 vertebra.

Resulting STL geometry was not representing a solid geometry, and L4 and L5 vertebrae were merged with each other. Moreover, there was also lots of geometry loss due to the variation in the CT scan voxel intensity. That geometry loss was fixed by using various editing tools in Meshmixer, and L4 and L5 were separated from each other.

As the next step, fixed STL geometries of L4 and L5 vertebrae was further prepared as a single enclosed surface, which is a necessity to obtain a solid geometry from the STL models. In order to prepare the vertebrae model for the IVD implementation, inferior end-plate of the L4 vertebrae, and superior end-plate of the L5 vertebrae was flattened. Prepared STL geometries of L4 and L5 vertebrae was given in Figure 2.3.

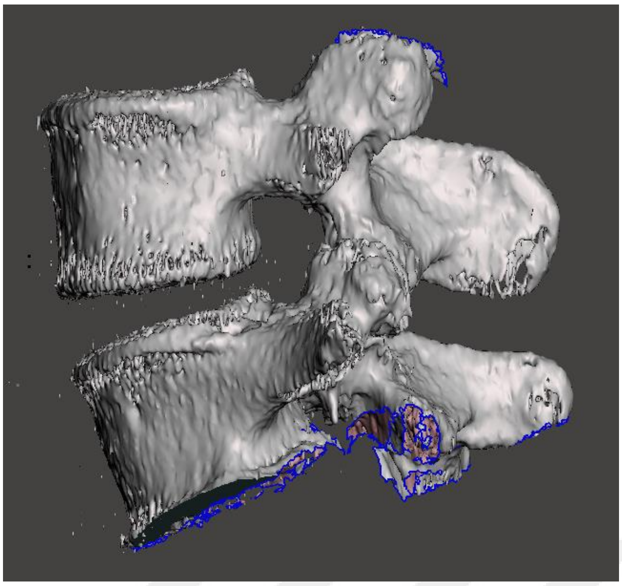

Figure 2.2. Illustration of the STL model of the L4 L5 spinal level from Autodesk Meshmixer.

As the final step, since the cancellous bone of the vertebral bodies has different material properties [14], in order to mesh that region separately, an inner shell for each vertebral body was generated (Figure 2.4.). Cortical bone thickness was assigned as 2mm, similar to the data reported in the literature [46].

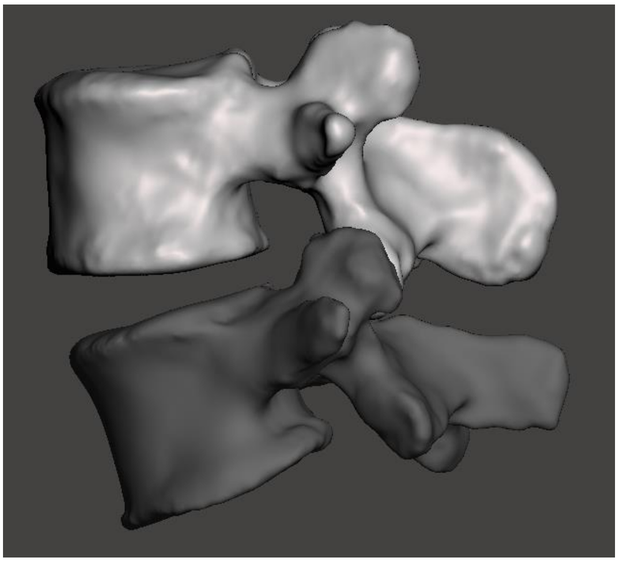

Figure 2.3. Edited the STL model of the L4 L5 spinal level, ready to be used to create a solid model.

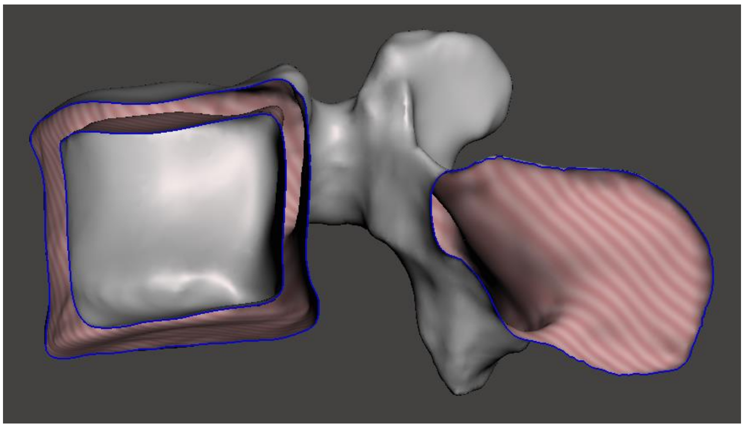

Figure 2.4. Sagittal plane cross-section of the L5 vertebrae STL.

In order to create solid geometry from the resulting STL models, we used Autodesk Fusion 360 version 2.0.8176. Resulting solid geometries were exported in Parasolid format, which is a well-known CAD data format that can carry solid geometry information [79]. Parasolid files were then imported to MSC Apex Jaguar for the meshing. Lower order linear tetrahedral elements used for the meshing since the geometry is too complicated to mesh with other element types [17]. 0.5-1mm mesh size was used for the meshing, as many other authors stated that they reached to mesh convergence between these values [53]. Mesh size was automatically decreased up to 0.5mm on more complex regions of the vertebrae during the automatic meshing process of MSC Apex Jaguar. An image of the meshed vertebrae of the segmented FE model is given in Figure 2.5.

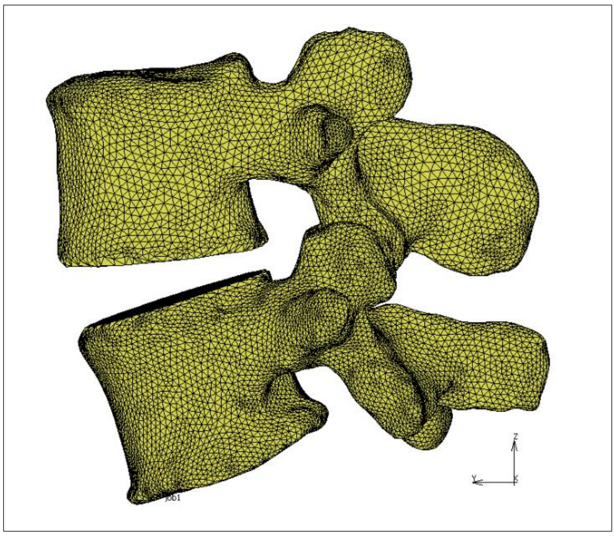

Figure 2.5. Meshed vertebrae of the segmented FE model.

2.1.2. Development of the Parametric FE Model Vertebrae

In order to develop the parametric FE model of the L4 L5 vertebral level, a previously developed parametric CAD model of the lumbar column was used [44]. Morphometric parameters required to generate that parametric CAD model were measured from the same patient’s CT scan that we used to develop the segmented FE model. Figure 2.6 illustrates the CAD model of L4 and L5 vertebrae of the mentioned parametric CAD model.

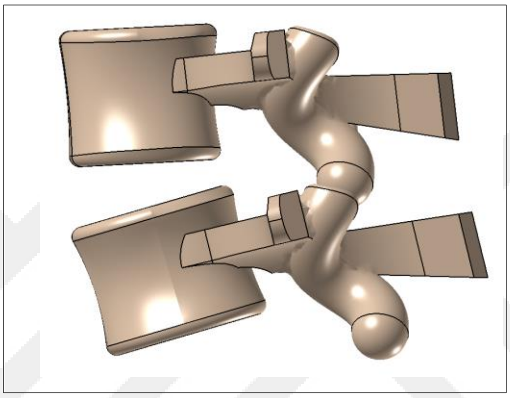

Figure 2.6. Parametric CAD model of the L4 L5 spinal level.

Since one of the reasons behind the idea of developing a parametric CAD model of the lumbar spine was to improve the mesh quality, we further divided each vertebra into two parts: vertebral body and posterior bony section. Therefore, the vertebral body was simplified enough to use hexahedral elements. However, the posterior bony section was still too complex to use the hexahedral element; therefore, similar to the segmented vertebra, we used tetrahedral elements for it again. Figure 2.7 further explains the diving procedure.

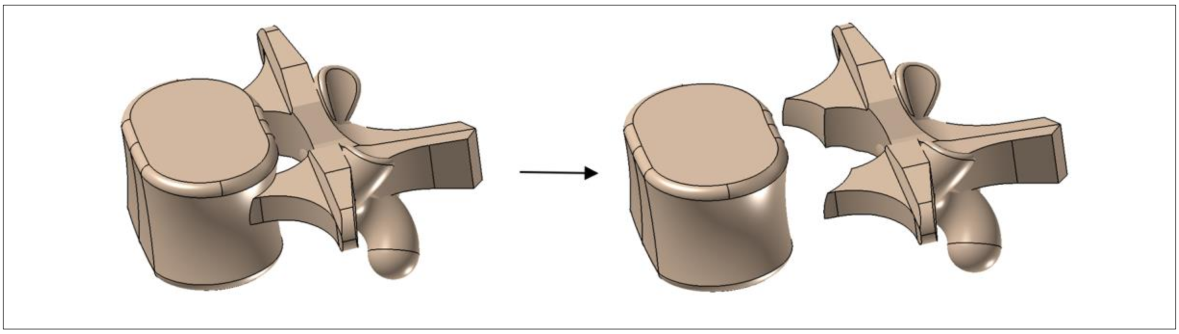

Figure 2.7. Two parts of the parametric CAD model of the vertebrae: vertebral body and posterior bony section.

Each vertebra meshed accordingly as the last step. MSC Apex Jaguar was used for the meshing procedure. 1-2mm mesh size was used for the meshing of the vertebral bodies. Lower order linear hexahedral elements were used for the meshing. As previously mentioned, the cancellous bone of the vertebral body has different material properties, and meshing had to be done accordingly to prepare an inner region ready to assign different material properties. Hexahedral meshing also helped to uniformly distribute the mesh elements, unlike tetrahedral meshing. Therefore, a proper region to assign different material properties was created indirectly through the hexahedral meshing process. Cortical bone thickness was again assigned as 2mm [46]. For the posterior bony section, similar to the segmented vertebra, lower order linear tetrahedral elements were used with a 0.5-1mm mesh size [53]. An image of the meshed vertebrae of the parametric FE model is given in Figure 2.8.

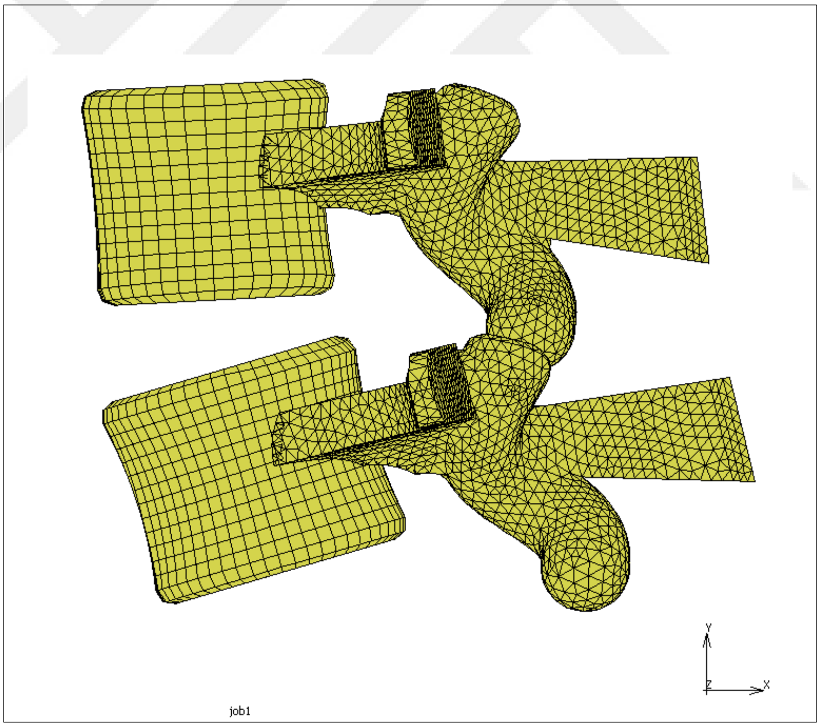

Figure 2.8. The meshed vertebrae of the parametric FE model.

2.2. DEVELOPMENT OF INTERVERTEBRAL DISC FE MODELS

In order to develop the FE model of the IVD for both the segmented and the parametric FE model, firstly, CAD models of the IVD was generated by using basic CAD geometry creation tools of Autodesk Fusion 360 version 2.0.8176. For both of our segmented and parametric FE models, we used loft operation to generate the IVD. The inferior end-plate surface of the L4 vertebrae and superior end-plate surface of the L5 vertebrae was connected to each other by using the loft operation. IVD bulge was neglected since it was causing distortions in the final mesh, which was directly affecting the anisotropic material properties of the annulus. The annulus and the nucleus volumes were shared through the IVD as 44 percent and 56 percent, respectively [14]. Finally, in order to create the annulus regions that have different material properties, the annulus was divided into four sections: anterior, posterior, and two lateral sections similar to the study published by Coombs et al. [18]. CAD models of the IVD for both the segmented and parametric FE models are given in Figure 2.9.

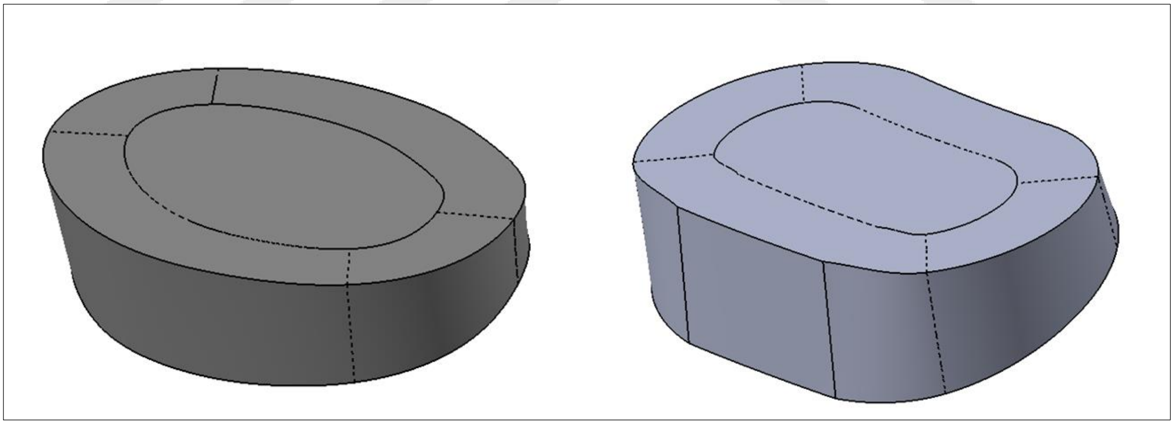

Figure 2.9. CAD models of the IVD models for both the segmented and parametric FE models, respectively.

IVD models meshed accordingly as the last step. MSC Apex Jaguar was used for the meshing procedure. 0.8mm mesh size was used for the meshing of the IVD, which is less than what has been suggested in the literature [53]. Lower order linear hexahedral elements were used for the meshing [17]. FE models of the IVD for both the segmented and parametric FE models are given in Figure 2.10.

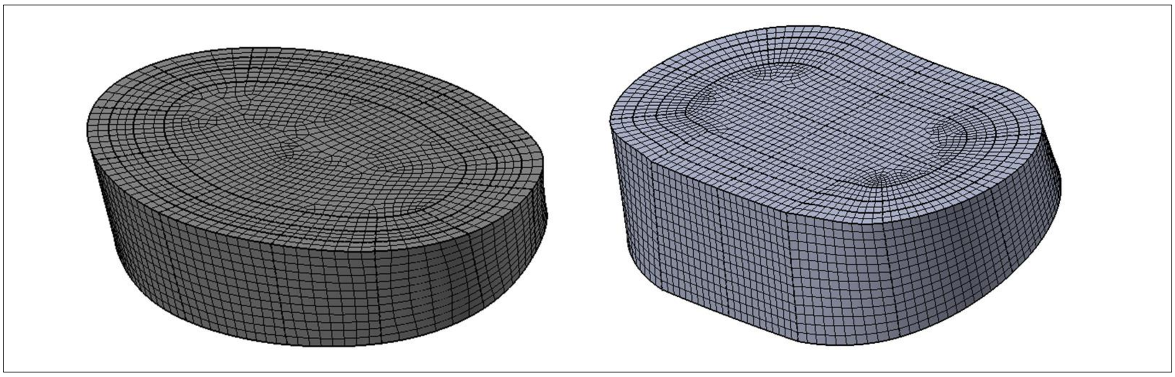

Figure 2.10. FE models of the IVD models for both the segmented and parametric FE models, respectively.

The coordinate system of the elements in the annulus sections was essential to adjust correctly because of the anisotropic nature of the annulus composite material properties. In order to arrange the element coordinate system continuity, a curvilinear coordinate system was used. The r-axis of each element was assigned to be towards the outer surface of the annulus, which automatically assigned the z-θ plane of each element to be tangential to the outer surface. The position of the z-θ plane was further defined by assigning the direction of the z-axis of each element towards from L5 vertebrae to the L4 vertebrae. Coordinate systems of each hexahedral elements of the annulus were adjusted accordingly to meet with this direction criteria. Coordinate systems of the annulus hexahedral elements were illustrated in Figure 2.11.

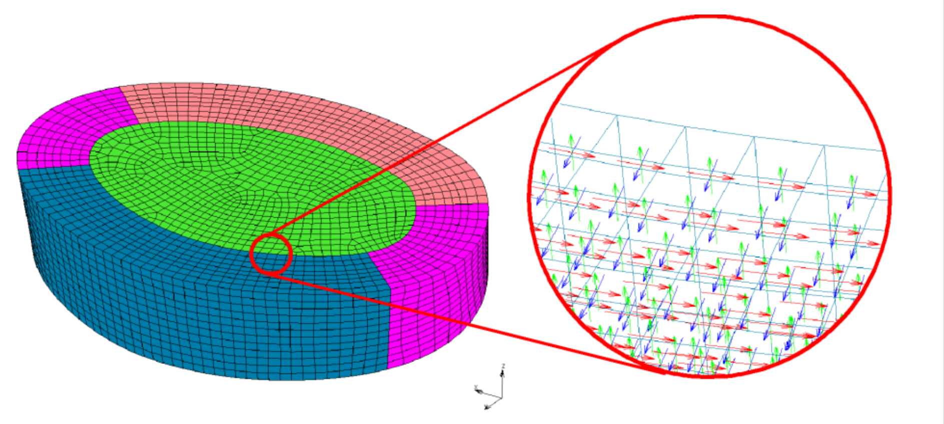

Figure 2.11. Coordinate system of the annulus hexahedral elements is illustrated for the parametric FE model.

2.3. MODELING OF LIGAMENT TISSUES

As mentioned previously, ligaments are biomechanical structures that mimic the behavior of a spring under tension, and provides force response accordingly, but behaves passively under compression [61]. In this study, we implemented that behavior by using 1-dimensional linear spring elements that behave as mentioned under tension and compression. Spring constants of the ligaments were obtained from the literature [18].

Seven different ligament tissues were included to both of our segmented and parametric FE models: anterior longitudinal ligament (ALL), posterior longitudinal ligament (PLL), supraspinous ligament (SSP), interspinous ligament (ISL), intertransverse ligament (ITL), facet capsular ligament (FCL) and ligamentum flavum (LFL) [18]. Ligament attachment sites were chosen based on the anatomic descriptions [54]. An illustration showing the one-dimensional elements representing the ligaments, and their attachment locations of each ligament was given in Figure 2.12.

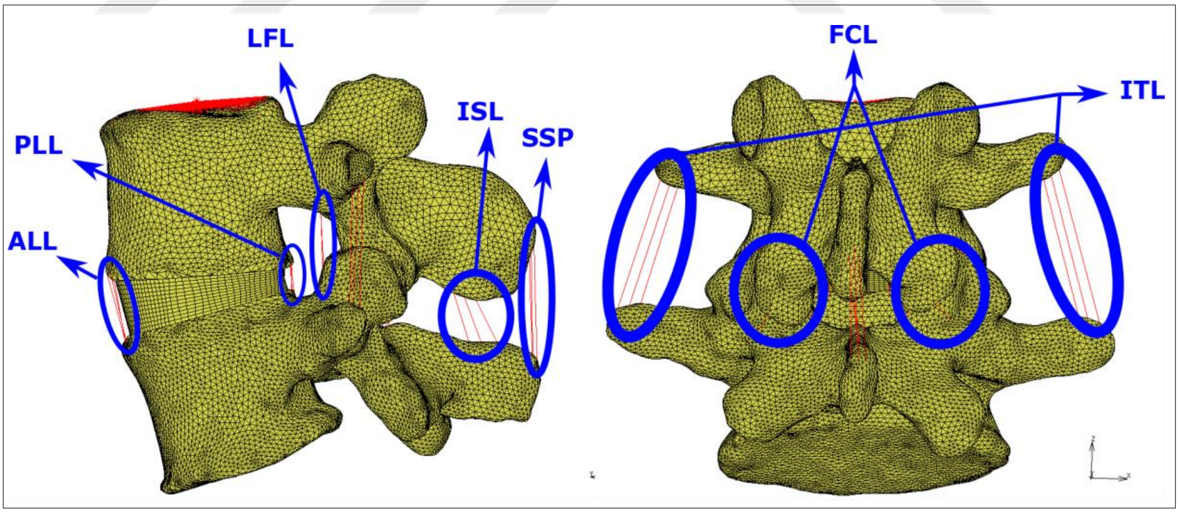

Figure 2.12. Spring elements representing the ligaments, and their attachment locations on the segmented FE model.

2.4. MATERIAL PROPERTIES AND ELEMENT TYPES

Vertebrae models were divided into three sections: cortical bone, cancellous bone, and posterior bony section. Each of these sections of the vertebrae assigned with linear elastic isotropic material properties [14]. The material properties of the vertebrae sections were given in Table 2.1 below.

Table 2.1. Material properties of the vertebrae sections [47].

	Young’s modulus (MPa)	**Poisson’s ratio (mm/mm)**
Cortical bone	12000	0.3
Cancellous bone	100	0.2
Posterior bony section	3500	0.25

As mentioned previously, tetrahedral elements were used for the segmented FE model vertebrae, whereas a combination of hexahedral and tetrahedral elements was used for the parametric FE model vertebrae. Element type 134 of Marc Mentat 2019 was used for the tetrahedral elements used on the vertebra. This element type uses linear interpolation functions while keeping the strains constant throughout the element, and only has one integration point on the centroid. For the hexahedral elements used on the vertebrae element type seven of Marc Mentat 2019 was used. This element type uses trilinear interpolation functions, and as a result, similar to the element type used for the tetrahedral elements, strains tend to be constant throughout the element. This element has eight integration points, which increases its stress and strain prediction accuracy over element type 134.

For the nucleus, linear elastic isotropic material properties were used. Element type seven of Marc Mentat 2019 that was also used for the hexahedral elements of the vertebrae, was again used for the nucleus. However, a smaller mesh size (0.8mm) was used for the nucleus to increase its non-linear prediction accuracy. Furthermore, since the nucleus itself behaves like a fluid, the nucleus material properties were defined with constant dilatation option, which forces the element to present incompressible behavior.

Contrary to vertebrae and the nucleus FE models, the annulus FE models of the IVD were modeled with much more complex material properties and element types. In order to mimic the fiber-reinforced hyperelastic composite behavior of the annulus tissue, a material with a general invariants-based strain energy density function was necessary. To accurately model that material behavior, hyperelastic anisotropic material properties with Holzapfel-Gasser-Ogden material formulation defined by four parameters (C_{10}, $k1$, $k2$, κ) having the following strain energy density function (U, given in Equation 2.1) was used [18]. This material formulation represents a phenomenological constitutive model that does not represent individual fibers and does not indicate the number of fibers. Volumetric behavior was defined to mimic the incompressible behavior by specifying an artificial Bulk Modulus as 125 GPa separately. That definition helped the convergence of the model and the development of the incompressible behavior. "κ" was defined as zero since fiber dispersion was not included in the model.

$$U = C_{10}(\bar{I}_1 - 3) + \frac{k1}{2k2}\sum_{i=1}^{n}\{exp[k2\bar{E}_i^2] - 1\}, \qquad i = 1, n \tag{2.1}$$

$$\bar{E}_i = \kappa\,(\bar{I}_1 - 3) + (1 - 3\kappa)(\bar{I}_4^{ii} - 1) \tag{2.2}$$

"C_{10}" is the shear modulus, which is a parameter that directly affects the stiffness of the matrix, whereas "$k1$" and "$k2$" affects the stiffness of the fibers, and determines the nonlinearity of the fibers, respectively. "κ" represents the fiber dispersion parameter. The number of reinforcing fiber families is represented by "n." "$\bar{I}_1$" stands for the volume-preserving part of the first invariant of the right or left Cauchy-Green deformation tensor. Lastly, "$\bar{I}_4^{ii}$" is one of the volume-preserving parts of two pseudo invariants measuring strain in the fiber directions. Lastly,"$\bar{E}_i$" represents the lagrange strain component through fiber direction.

Two fiber layers throughout the element with two reinforcing fiber families per layer was defined with the fiber orientations obtained from the literature [53]. Fiber orientations were defined in the z-θ plane, where the θ-axis and z-axis represent 0 and 90-degree fiber orientations, respectively. Fiber orientations and layers were approximately normal to the radial direction (thickness direction) of the annulus tissue. Thus during the meshing step, all the element coordinate systems were aligned accordingly. Similar to the nucleus, since the annulus also showed incompressible behavior, the annulus material properties were defined with constant dilatation option. Element type 149 of Marc Mentat 2019 was used for the hexahedral elements of the annulus. This element is defined as an isoparametric, 8-node composite brick, for which different material properties can be defined in different layers within the element. Each layer of this element carries four integration points. An illustration describing the composite layers of each the annulus element and its direction is shown in Figure 2.13. Material properties for both the nucleus and the annulus are given in Table 2.2.

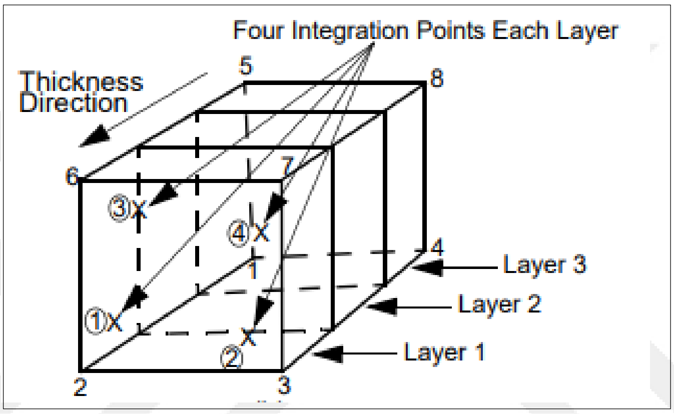

Figure 2.13. Illustration of the element type 149.

Table 2.2. Material properties of the IVD [31, 53].

The annulus:	**Matrix**		**Fibers**	**Anterior**	**Lateral**	**Posterior**
	C_{10} **(MPa)**	0.25	$k1$ **(MPa)**	2	3	5
	Bulk modulus (GPa)	125	$k2$	190	45	10
			Angle (deg.)	26	34.9	43
			κ	0	0	0
The nucleus:	**Young's modulus:**	1 MPa				
	Poisson's ratio:	0.49				

In order to define the spring-like nature of the intervertebral ligament tissue, a mean value of the stiffness data from the literature was used. The mean values of the stiffness and their standard deviations are given in Table 2.3 below.

Table 2.3. Stiffness values of the ligaments [18].

	Mean	**Standard deviation**
ALL Stiffness (N/mm)	55.39	17.87
PLL Stiffness (N/mm)	31.3	22.48
LFL Stiffness (N/mm)	23.23	8.67
FCL Stiffness (N/mm)	30.6	1.5
ITL Stiffness (N/mm)	35.35	7.2
ISL Stiffness (N/mm)	24.68	15.75
SSP Stiffness (N/mm)	20.55	9.96

2.5. ANALYSIS SETUP AND BOUNDARY CONDITIONS

As the next step, FE models of the vertebrae and IVD of both segmented and parametric FE models were imported to Mentat 2019. In Mentat, one-dimensional elements representing the ligament tissues were defined, contact relations were assigned, and the analysis setup was prepared. All the simulations were performed on Marc Mentat 2019. This software was preferred because of its superior non-linear solving capabilities. Full Newton-Raphson iterative procedure was used during the solution. In order to test the convergence during each step, relative residual forces and moments, as well as relative displacements were used. This convergence testing approach is known to be well-behaving for highly non-linear problems such as ours. In order to further improve the convergence of the analysis, applied loads were divided into 100 equal steps, and the load was increased incrementally. The large strain option was used in the non-linear solution parameters.

Contact interactions between the bodies were defined in a contact table. Contact interaction between vertebral bodies and IVDs was defined with glue contact interaction without separation, which inseparably bonds the bodies to each other. On the other hand, posterior bony sections were defined with touching contact interaction since they are touching each other at the facet joints. Facet joints of the lower and upper segments of the vertebrae are separable from each other without any reaction force but are kept intact with the FCL ligaments.

As the last step, boundary and loading conditions were defined. The boundary condition in the inferior end-plate of the L5 vertebrae and its inferior facet joints were completely fixed from moving in all degree-of-freedoms. In order to define the loading, a supernode on the superior end-plate of the L4 vertebrae was created, and all the nodes in the superior end-plate of the L4 vertebrae were connected to that node with rigid body elements (named as RBE2 elements in Marc Mentat 2019). This supernode is referred to as the loading node in the remaining part of our text. The motion tasks that were applied were flexion, extension, lateral bending, and axial rotation. For each one of these tasks, a 10 Nm pure-moment load was applied to the loading node [18, 53]. Rigid body elements connecting the superior end-plate nodes of the L4 vertebrae to the loading node-enabled a distribution of the pure-moment load to the superior end-plate of the L4 vertebrae. Boundary and loading conditions are illustrated in Figure 2.14.

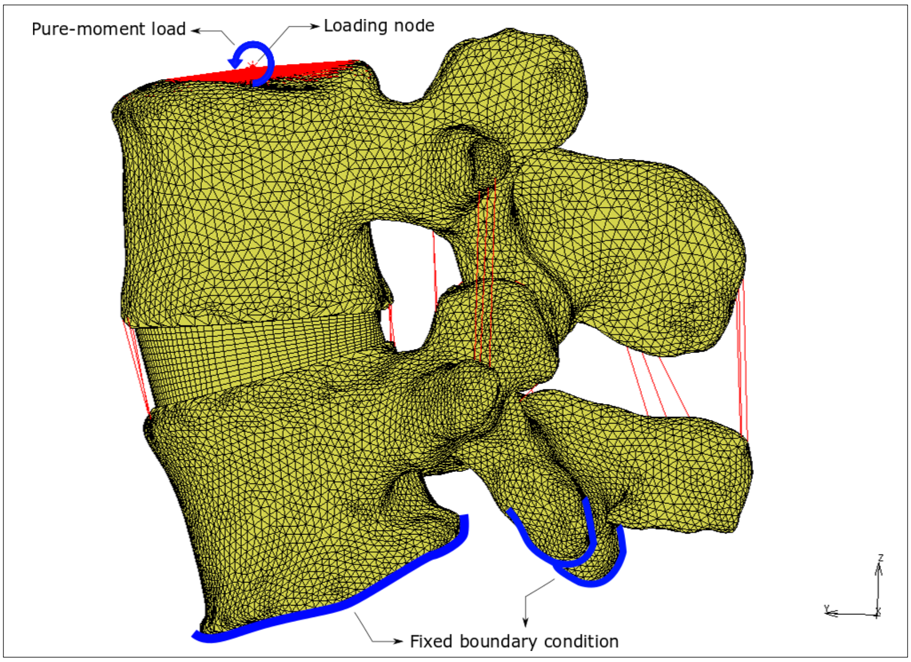

Figure 2.14. Illustration of the boundary conditions and the loading.

2.6. VERIFICATION AND VALIDATION

Just as stated by many previous authors, mesh density is an essential parameter for verification that is directly related to the FE model predictions, and solution accuracy [66]. Therefore, in order to understand how reliable the FE results are, and verify them, the mesh density factor must also be considered as an important indicator of convergence [64]. In this study, we performed two different mesh convergence studies for the intervertebral disc: (1) for the whole intervertebral disc, and (2) for the annulus tissue only. For each approach, mesh size was decreased by one half, starting from 5mm up to 0.15mm where possible. After that, an extensive validation process was performed by comparing our results with the data reported in the literature.

2.6.1. Intervertebral Disc Convergence Study

In order to perform the mesh convergence study, a simplified cylindrical FE model of the intervertebral disc was created (Figure 2.15), and subjected to 10 Nm pure moment load on its top surface, while keeping the bottom surface fixed from all its degree-of-freedoms. As mentioned in the previous sections, the annulus tissue is modeled as an incompressible hyperelastic fiber-reinforced material. Moreover, as shown in Holzapfel et al. [58], the fiber alignment is a function of the circumferential position around the annulus as well as a function of radial position. In the annulus model that was used in the convergence study, anterior the annulus material properties were used for the whole the annulus tissue. The relative error of the FE model outputs was compared with respect to each other as the models were successively refined by reducing the element size.

In order to observe the range of motion convergence, maximum x-axis displacement data from the node where the maximum compression occurred was collected from the annulus and the nucleus separately. Similarly, from the same nodes, in order to observe the stress convergence, the maximum first principal component of the Cauchy stress data from the annulus and the nucleus was collected.

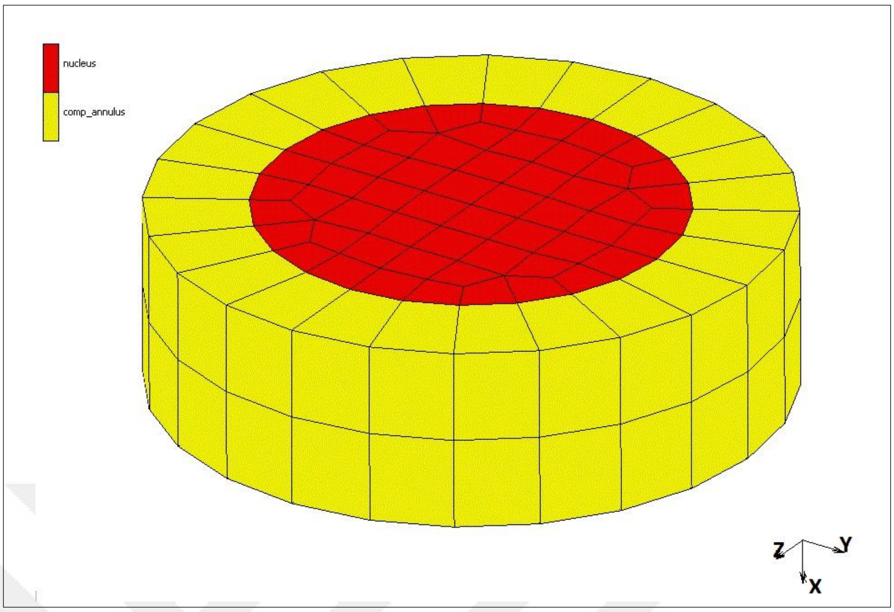

Figure 2.15. Simplified cylindrical FE model of the intervertebral disc.

To calculate the relative error, resulting data for that mesh size was subtracted from the data collected from one previous mesh size and divided into that. Therefore for every two data, one relative error value was calculated and presented as a percentage. The formula for the relative error calculation was presented in Equation 2.3.

$$RE_{i,i-1} = 100\% \times \frac{(D_i - D_{i-1})}{D_{i-1}} \tag{2.3}$$

In this equation, RE_i stand for the relative error, and D_i stands for the collected data. The subscript i represents the models developed for the convergence study in a decreasing mesh size order.

Maximum x-axis displacement and the first component of principal Cauchy stress values, as well as their relative error values calculated by this approach for both the annulus and the nucleus, were reported in the results section.

2.6.2. The Annulus Convergence Study

The annulus fibrosus tissue was simplified further up to a ring geometry where the analytical comparison is possible (Figure 2.16). A polar coordinate system was used for this study. 0.5 MPa inner pressure was applied from the inner surface of the ring through the negative normal direction. The bottom surface of the ring was only allowed to move in the radial axis direction, whereas the top surface was allowed to move in the radial axis and z-axis direction.

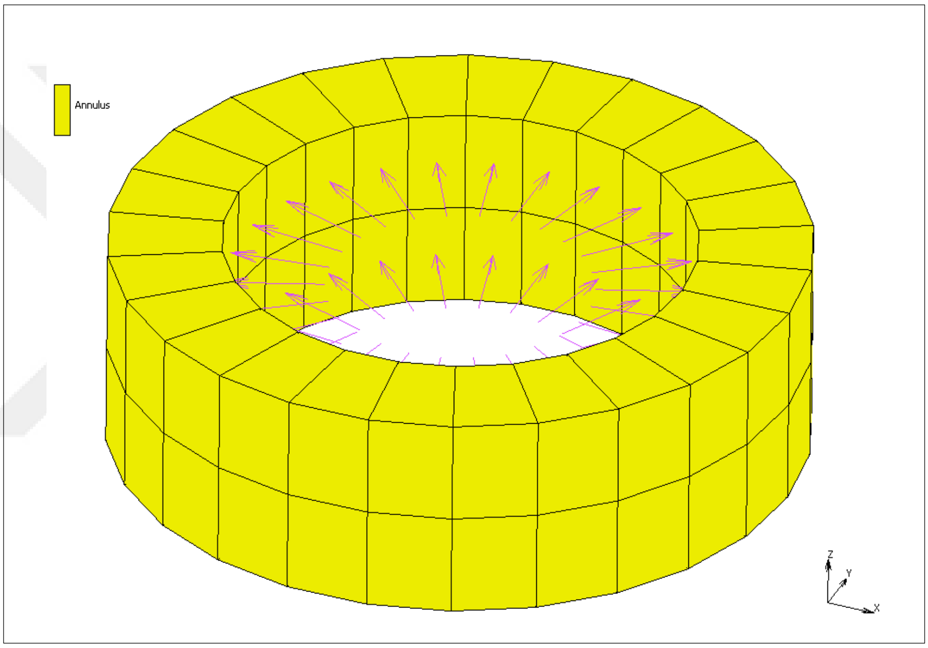

Figure 2.16. Ring geometry as a simplified version of the annulus tissue.

Analytically, it is a known fact that when a hollow cylinder was subjected to an inner pressure, radial stresses in the inner wall would be equal to the subjected inner pressure, which gradually decreases through the outer surface (Figure 2.17). Therefore, under 0.5 MPa inner pressure, it is expected to observe 0.5 MPa radial stress values (σ_r) in the inner surface of the ring. In this convergence study, for each mesh size, we calculated the relative error values of the radial Cauchy stress results by comparing it with our analytical expectancies. The formula for the error calculation was presented in Equation 2.4.

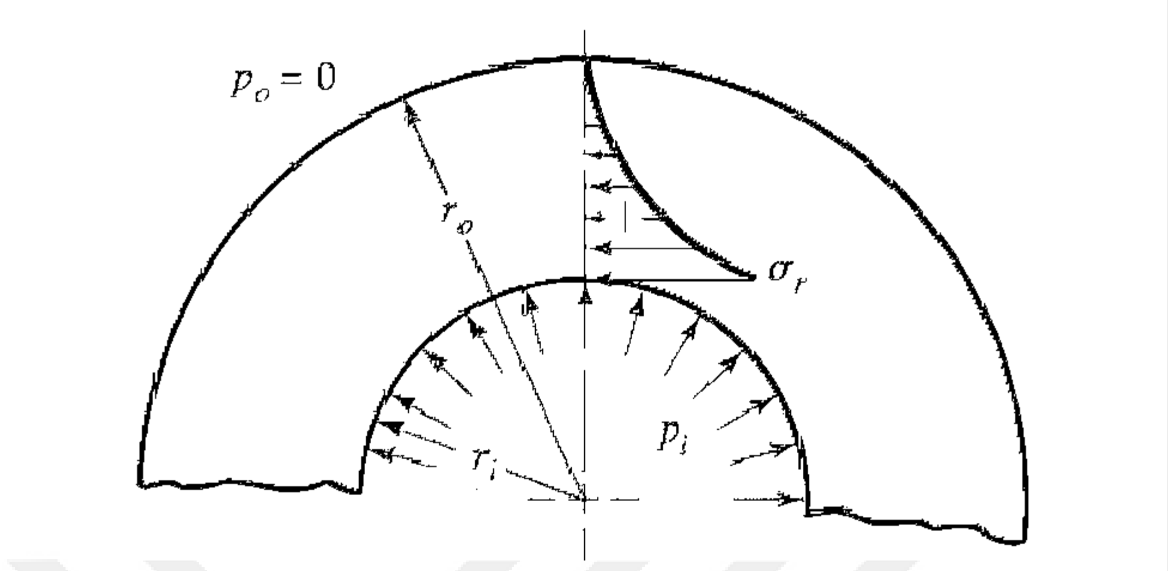

Figure 2.17. Stress distribution of a hollow cylinder under inner pressure.

$$RE_{i,-0.5MPa} = 100 \times \frac{(-0.5\ MPa - D_i)}{D_i} \tag{2.4}$$

In this equation, $RE_{i,-0.5MPa}$ represents the error value relative to -0.5MPa analytical expectancies, while D_i represents the collected data for that specific mesh size, i.

Even though the radial Cauchy stress output of this model can be estimated by analytical approaches, the same approach is not valid for displacements because of the non-linear nature of the annulus material. Therefore, in addition to error calculations relative to the analytically obtained radial Cauchy stress, relative error of radial displacement was also calculated for this study and reported in the results section.

2.6.3. Validation

In the literature, the three main response parameters that were most frequently used in order to validate the FE models of the lumbar spine are the moment-rotation curves, the intradiscal nuclear pressures, and facet joint contact forces [31, 53]. Therefore we also applied these parameters in validating our segmented and parametric FE models.

In order to draw the moment-rotation curve, nodal rotation along the moment axis was collected from a node on the superior end-plate of the L4 vertebrae, and it was plotted against the external moment applied. FJF was calculated as the vector summation of nodal contact forces at the facet contact region. As there was no available fluid element definition in Marc Mentat 2019, similar to a previously developed FE model of the lumbar spine [30], we used an isotropic incompressible material for the nucleus with the material properties listed in the previous sections. In order to collect the IDP data, the mean hydrostatic pressure was calculated by summing the principal Cauchy stresses at each node and then calculating the mean and standard deviation of this set of values [80]. This mean hydrostatic pressure was accepted as the IDP of the nucleus.

The moment-rotation curve, IDP, and FJF were found on both the segmented and the parametric FE models corresponding to different motion tasks and were compared with the experimental and FE model data from the literature.

3. RESULTS

For the verification part of our study convergence test results, and for the validation part; moment-rotation curves, IDPs, and FJFs for both model was provided, and compared with the other models, as well as with the experimental data reported.

3.1. VERIFICATION

The verification of computational models are generally divided into two: code verification and calculation verification [66]. The Code verification process is generally performed by the software companies whose products are on use to develop such models [73, 74]. Calculation verification, on the other hand, is mostly necessary to understand whether the discretization level of the problem accurately represents the geometry. In order to complete that step, mesh convergence studies are performed.

3.1.1. Mesh Convergence Study Results

Mesh convergence study provided a comprehensive view for us to choose the mesh size of our study, and understand the reliability of our models by providing error values. We performed two different mesh convergence studies for the intervertebral disc: (1) for the whole intervertebral disc, and (2) for the annulus tissue only. For each approach, mesh size was decreased by one half, starting from 5mm up to 0.15mm where possible.

3.1.1.1. Intervertebral Disc Convergence Study Results

Maximum x-axis displacement values for both the annulus and the nucleus from the node where the maximum compression occurred was calculated and reported in Figure 3.1. In this figure, these results were reported for each mesh size. The relative error of displacement for both the annulus and the nucleus was also calculated and reported for each mesh size together in a separate Figure 3.2. The first component of the principal Cauchy stress from the node where the maximum compression occurred and its relative error calculations was also calculated and reported in a similar manner in Figure 3.1 and 3.2, respectively. In each figure, a table representing the data was also provided for further understanding.

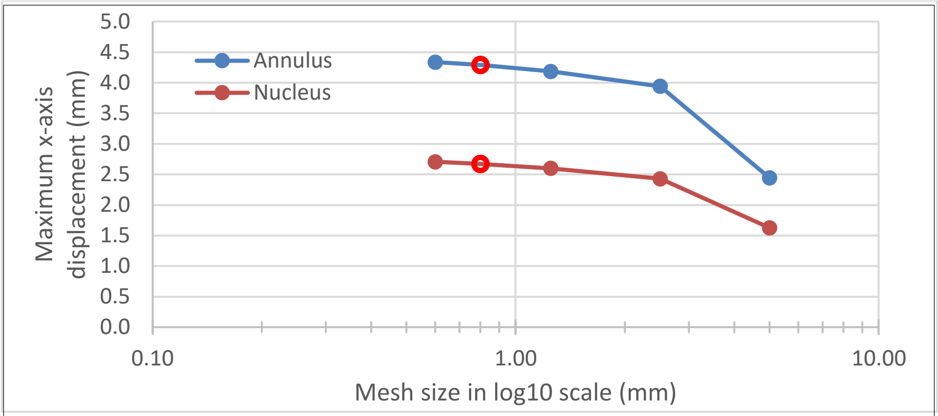

Mesh size (mm)	Maximum x-axis displacement (mm)	
	The annulus	The nucleus
5.00	2.445	1.626
2.50	3.941	2.430
1.25	4.185	2.599
0.80	4.290	2.672
0.60	4.338	2.708

Figure 3.1. Line graph of maximum x-axis displacement for both the annulus and the nucleus with respect to mesh size, and table presenting the data used for the graph.

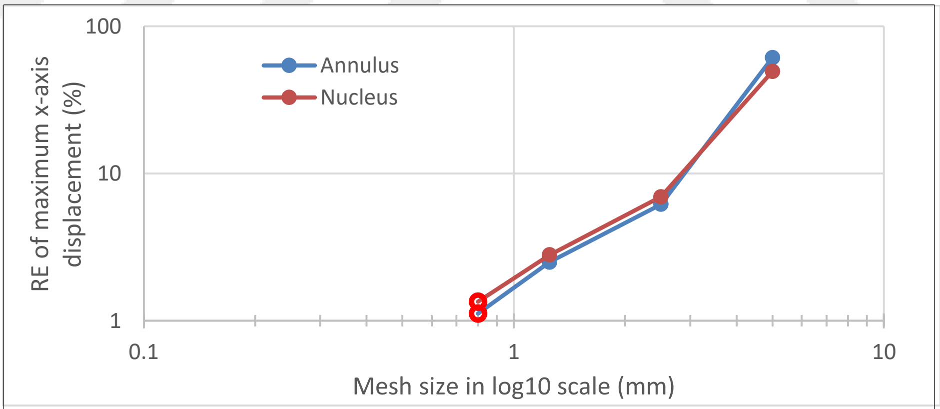

Mesh size (mm)	RE of maximum x-axis displacement (%)	
	The annulus	The nucleus
5.00	61.186	49.446
2.50	6.191	6.955
1.25	2.509	2.809
0.80	1.119	1.347

Figure 3.2. Line graph of relative error ($\boldsymbol{RE_{i,i-1}}$) of maximum x-axis displacement for both the annulus and the nucleus with respect to mesh size, and table presenting the data used for the graph.

In Figures 3.1 and 3.2, it is observed that after 2.5mm mesh size, maximum x-axis displacement converged to approximately 4.5mm for The annulus and 3mm for the nucleus, with an error below 1.5 percent for both. Mesh size below 2.5mm was found to produce well-converged displacement results. Therefore, 0.8mm mesh size used in this study was also confirmed well-converged in terms of displacement outputs with 1.1 percent and 1.3 percent relative error values for The annulus and the nucleus, respectively. Red circular data point represents the mesh size used in this study.

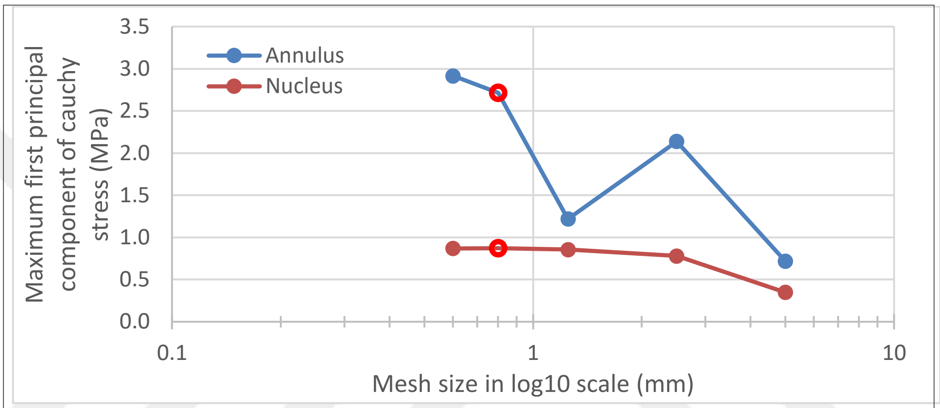

Mesh size (mm)	The maximum first principal component of Cauchy stress (MPa)	
	The annulus	The nucleus
5.00	0.716	0.347
2.50	2.138	0.779
1.25	1.219	0.856
0.80	2.715	0.872
0.6	2.916	0.868

Figure 3.3. Line graph of maximum first principal component of cauchy stress for both the annulus and the nucleus with respect to mesh size, and table presenting the data used for the graph.

In Figures 3.3 and 3.4, the first principal component of Cauchy stress of the nucleus started to converge between 0.86 and 0.87 MPa below 1.25mm mesh size, while relative error values of it were between 1.8 and 0.4 percent. 0.8mm mesh size used in this study was provided 0.4 percent relative error values for equivalent Cauchy stress values of the nucleus. With a 0.4 percent relative error, 0.8mm mesh size that we used in this study was found reliable for equivalent Cauchy stress calculations of the nucleus.

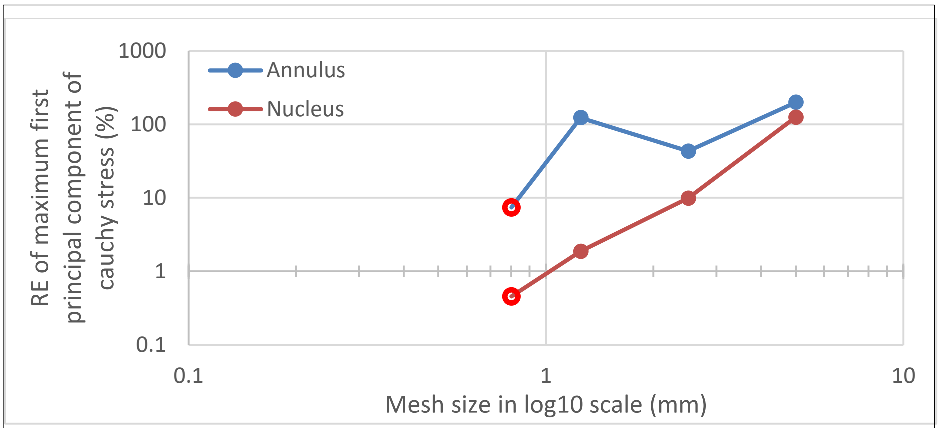

Mesh size (mm)	RE of the maximum first principal component of Cauchy stress (%)	
	The annulus	The nucleus
5.00	198.603	124.495
2.50	42.984	9.884
1.25	122.72	1.869
0.80	7.403	0.458

Figure 3.4. Line graph of relative error $(\boldsymbol{RE_{i,i-1}})$ of maximum first principal component of cauchy stress for both the annulus and the nucleus with respect to mesh size, and table presenting the data used for the graph.

The first principal component of Cauchy stress of the annulus was observed to be showing an increasing behavior. After 1.25mm mesh size first principal component of Cauchy stress was observed to be increasing rapidly from approximately 1.2 to 2.9 MPa, with relative error values was found to be higher than expected. For the annulus, a further decrease in the mesh size was seemed necessary in order to obtain more reliable relative error values; however, due to computational limitations, a further decrease in the mesh size was not possible.

3.1.1.2. The Annulus Convergence Study Results

The maximum radial displacement values of the simplified the annulus model were reported in Figure 3.5. In this figure, total displacement values were reported for each mesh size. The relative error of maximum radial displacement was reported for each mesh size in Figure 3.6. Maximum radial Cauchy stress values and its relative error calculations were also calculated and reported in a similar manner in Figure 3.5 and 3.6, respectively. In each figure, a table representing the data was presented in the figure for further understanding. The red hollow data point in the figures represents the 0.8mm mesh size used in segmented and parametric FE models. Red circular data point represents the mesh size used in this study.

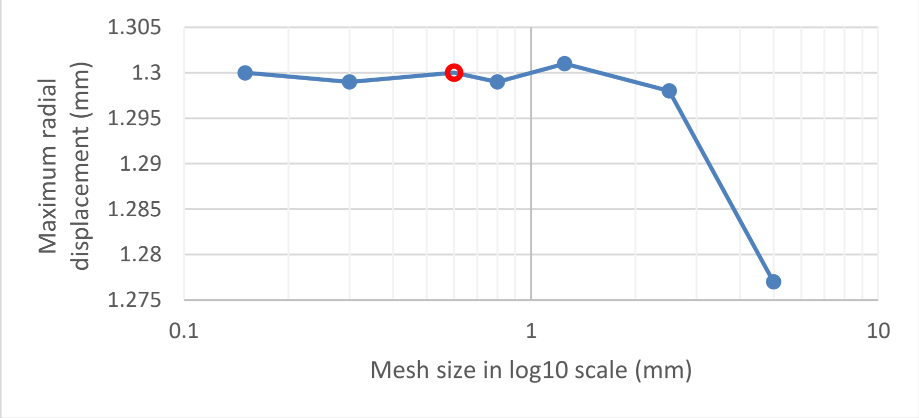

Mesh size(mm)	**Maximum radial displacement (mm)**
5	1.277
2.5	1.298
1.25	1.301
0.8	1.299
0.6	1.300
0.3	1.299
0.15	1.300

Figure 3.5. Line graph of maximum radial displacement of the simplified the annulus with respect to mesh size, and table presenting the data used for the graph.

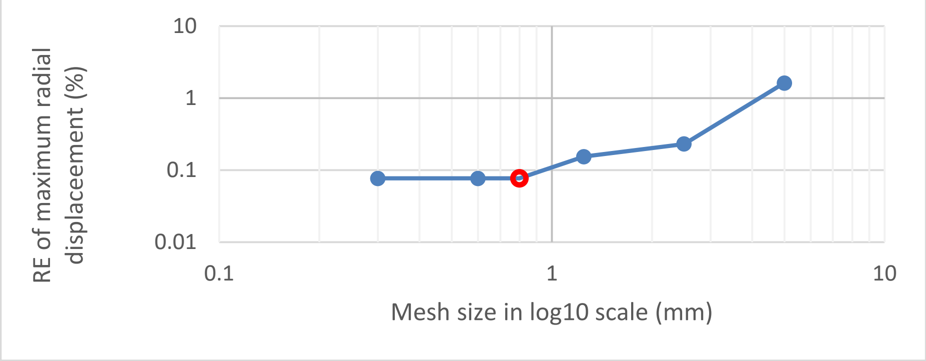

Mesh size(mm)	RE of maximum radial displacement (%)
5	1.644
2.5	0.231
1.25	0.153
0.8	0.077
0.6	0.077
0.3	0.077

Figure 3.6. Line graph of relative error ($\boldsymbol{RE_{i,i-1}}$) of maximum radial displacement of the simplified the annulus with respect to mesh size, and table presenting the data used for the graph.

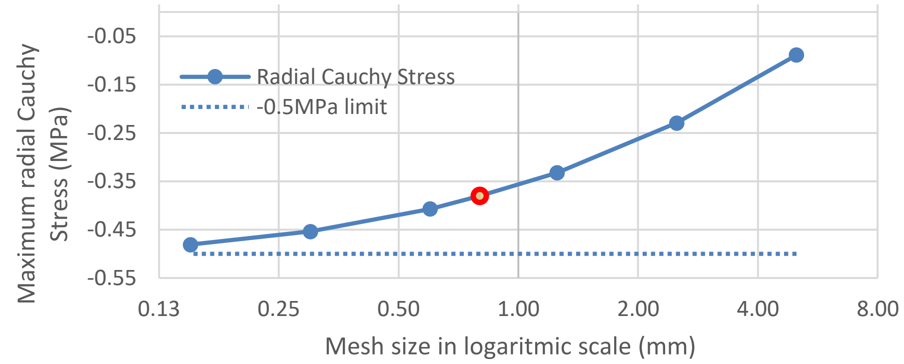

Mesh size (mm)	Maximum radial Cauchy stress (MPa)
5.00	-0.09
2.50	-0.23
1.25	-0.33
0.80	-0.38
0.60	-0.41
0.30	-0.45
0.15	-0.48

Figure 3.7. Line graph of maximum radial cauchy stress of the simplified the annulus with respect to mesh size, and table presenting the data used for the graph.

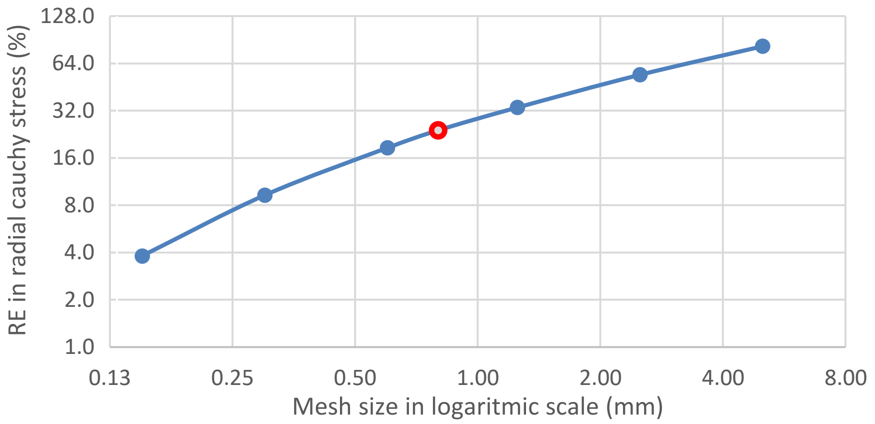

Mesh size (mm)	The relative error of radial Cauchy stress (MPa)
5	82.2
2.5	54.1
1.25	33.5
0.8	24.0
0.6	18.5
0.3	9.3
0.15	3.8

Figure 3.8. Line graph of relative error ($\boldsymbol{RE_{i,-0.5\,MPa}}$) of maximum radial cauchy stress of the simplified the annulus with respect to mesh size, and table presenting the data used for the graph.

In Figures 3.5 and 3.6, it is observed that after 1.25mm mesh size, radial displacement was converging to approximately 1.3mm with a relative error below 0.1 percent. Mesh size below 1.25mm was found to produce well-converged displacement results. Therefore, 0.8mm mesh size used in this study was again confirmed reliable for the annulus in terms of displacement outputs.

In Figures 3.7 and 3.8, equivalent Cauchy stress values for the annulus was observed to be converging to 0.5MPa, as expected. Relative error values were also observed to be converging to zero percent with every decrease in the mesh size. 0.8mm mesh size used in this study was provided 24 percent relative error values for radial Cauchy stress.

Compared to the previous sensitivity study, since this approach does not include the nucleus, the number of elements used for this study decreased dramatically. Therefore we were able to decrease the mesh size even further. Relative error values for 0.8mm were found to be higher than expected, with 24 percent. Calculated results also correlate with the results of the previous convergence study.

3.2. VALIDATION

3.2.1. Moment-Rotation Curve

Moment-rotation response of the segmented and parametric FE model for flexion/extension, lateral bending, and axial rotation is given together in Figures 3.9, 3.10, and 3.11, respectively. In these figures, experimental data by Guan et al., and Campbell et al. [81, 82], and FE data validated by Coombs et al., and Rao et al. [18, 83] was also included for the validation purposes. Both experimental data were collected under the same boundary and loading conditions with our study and represent the experimental interval with ±1 degree standard deviation due to human error. Note that data provided by Guan et al. [81] was limited to 4Nm pure-moment loading, a comparison was only possible within this region.

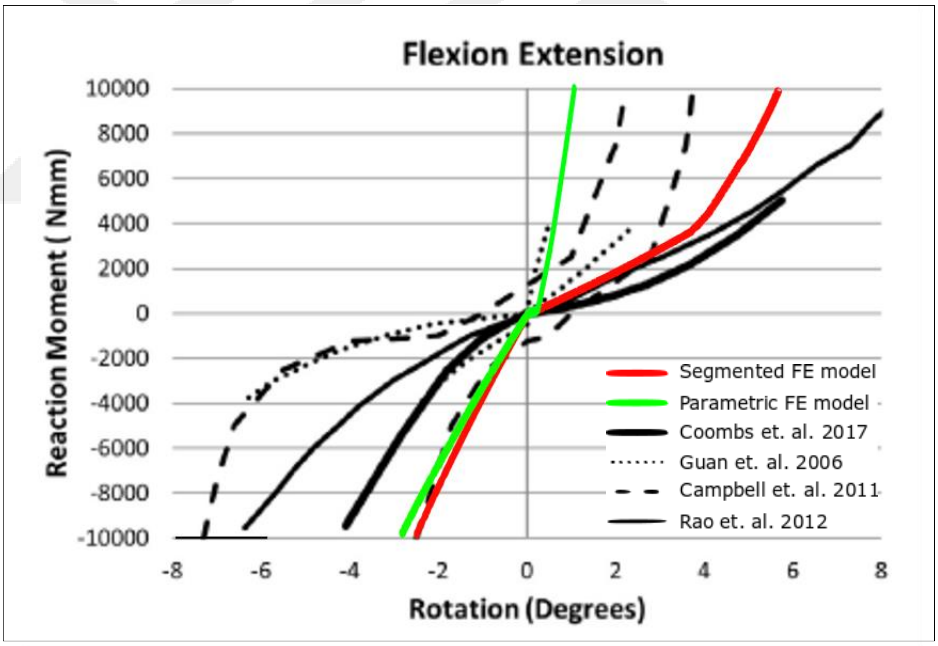

Figure 3.9. Comparison of moment-rotation curves of segmented (red), and parametric (green) FE models for flexion (negative side of the rotation axis), and extension (positive side of the rotation axis) with data from the literature [18, 81–84].

For flexion, maximum rotation along the applied moment axis was observed as 2.50 and 2.74 degrees for segmented and parametric models, respectively. Moment-rotation curves of both segmented and parametric FE model results showed similar behavior. Their angular difference at –10 Nm was calculated as 9 percent.

Comparing the flexion moment-rotation curve of both parametric and segmented FE models with the literature, it was observed that these FE models fell within the experimental data range of Campbell et al. [82]. However, their response were outside of the experimental data range provided by Guan et al. [81]. All the experimental and FE curves provided for flexion were observed to follow a similar pattern, which indicated that our models were captured the actual response of the spine under flexion.

For extension, maximum rotation along the applied moment axis was observed as 5.56 and 1.09 degrees for segmented and parametric models, respectively. Unlike flexion, moment-rotation curves of these FE model results were not similar. Their angular response differed by 410 percent under +10 Nm.

Comparing the extension moment-rotation curve of our FE models with the literature, it was observed that the segmented FE model result fell outside of both experimental response data (Campbell et al. [82] and Guan et al. [81]). Segmented FE model was observed to be more compliant compared to both of these experimental data. On the other hand, parametric FE model result fell within the experimental data range of Guan et al. [81], while it behaved stiffer than Campbell et al. [82].

In terms of the final rotation angle and the curve behavior, the segmented FE model was observed to be capturing the actual response of the spine under extension more accurately; however parametric FE model fell far outside of the range. Even though the curve patterns were similar to other presented studies, parametric FE model results were observed to be stiffer than the reality. It was also observed that for the facets of the segmented FE model contact occurred after approximately four degrees of rotation, while for the facets of the parametric model contact occurred almost instanteneously following the start of the motion task. This was the reason why the parametric model behaved much stiffer compared to the segmented FE model.

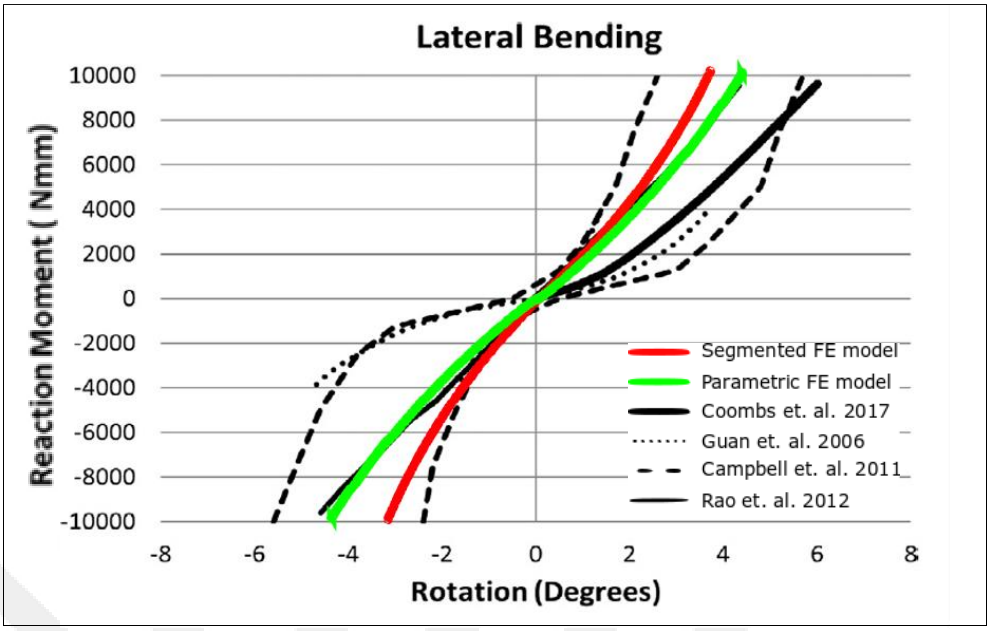

Figure 3.10. Comparison of moment-rotation curves of segmented (red), and parametric (green) FE models for lateral bending with the literature [18, 81–84].

For lateral bending, maximum rotation along the applied moment axis was observed as 3.75 and -3.42 degree for the segmented FE model, and ±4.44 degree (because of symmetry) for the parametric FE model. Moment-rotation curves of both segmented and parametric FE model results showed similar behavior to each other. Their angular difference under ±10 Nm was calculated as 18 percent and 30 percent. The parametric model behaved more compliant than the segmented FE model in lateral bending. The asymmetry of the segmented FE model geometry highly affected the model predictions in lateral bending. Note that parametric FE model was perfectly symmetric with respect to the sagittal plane.

Comparing the lateral bending moment-rotation curve of both parametric and segmented FE models with the literature, it was observed that these FE models fell within the experimental data range of both Campbell et al. [82] and Guan et al. [81]. In addition, a good agreement was observed between our FE model results and other FE study results of Rao et al. and Coombs et al. [18, 83]. All the experimental and FE curves provided for lateral bending were observed to be following a similar pattern which indicated that our models were capturing the actual behavior of the spine under lateral bending.

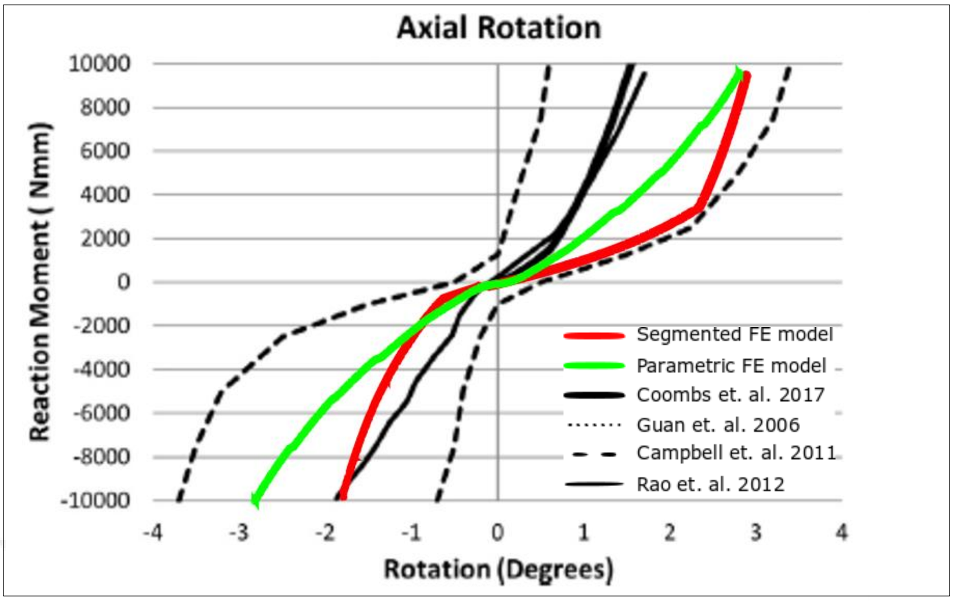

Figure 3.11. Comparison of moment-rotation curves of segmented (red), and parametric (green) FE models for axial rotation with the literature [18, 81–84].

For axial rotation, maximum angle along the applied moment axis was observed as 2.83 and -1.70 degree for the segmented FE model, and ±2.80 degree for the parametric FE model. Moment-rotation curves of these FE model results did not show similar behavior. The difference between rotation responses under ±10 Nm was calculated as 1 percent and 40 percent. Similar to lateral bending, the non-symmetric nature of the segmented FE model was observed to be highly affecting the model predictions in axial rotation.

Comparing the axial rotation moment-rotation curve of both parametric and segmented FE models with the literature, it was observed that these FE models fell within the experimental data range of both Campbell et al. [82] and Guan et al. [81]. In addition, a good agreement was observed between our FE model results and other FE study results of Rao et al. and Coombs et al. [18, 83]. Our model results were observed to be slightly less stiffer than the other FE model results. All the experimental and FE curves were observed to be following a similar pattern, which indicated that our models were capturing the actual behavior of the spine in axial rotation.

Maximum rotation values from Figures 3.9, 3.10, and 3.11 have been compiled in Table 3.1 where both segmented and parametric FE models in flexion/extension, lateral bending, and axial rotation are listed.

Table 3.1. Maximum moment-rotation responses of the segmented and parametric FE model under ±10 Nm pure moment load. “L” indicates a movement through the left lateral side, while “R” indicates the opposite, and “S” indicates the symmetry where the left and right results are the same.

	Rotation values under pure-moment loads (degree)		
	Segmented		**Parametric**
Flexion (-10 Nm)	2.51		±2.74
Extension (10 Nm)	5.57		±1.09
Lateral bending (±10 Nm)	3.75 (L)	-3.43 (R)	±4.44 (S)
Axial rotation (±10 Nm)	2.83 (L)	-1.70 (R)	±2.80 (S)

3.2.2. Intradiscal Nuclear Pressure Response

The nucleus hydrostatic pressure nodal response distributions of the segmented and parametric FE model for flexion, extension, lateral bending, and axial rotation are shown together in Figures 3.12, 3.13, 3.14, and 3.15, respectively. IDP results of both segmented and parametric FE models were validated with the experimental data from the literature [30, 85].

For flexion, the mean value of the total nodal hydrostatic pressures were calculated as 0.36 and 0.32 MPa for segmented and parametric FE models, respectively. The relative error of mean values between these FE models was 12 percent. Standard deviations were calculated as 0.09 MPa for the segmented, and 0.04 MPa for the parametric FE model. We note that a slightly wider variability was observed in the segmented FE model. In summary, hydrostatic pressure calculation of segmented and parametric FE models were observed to be in good agreement for flexion.

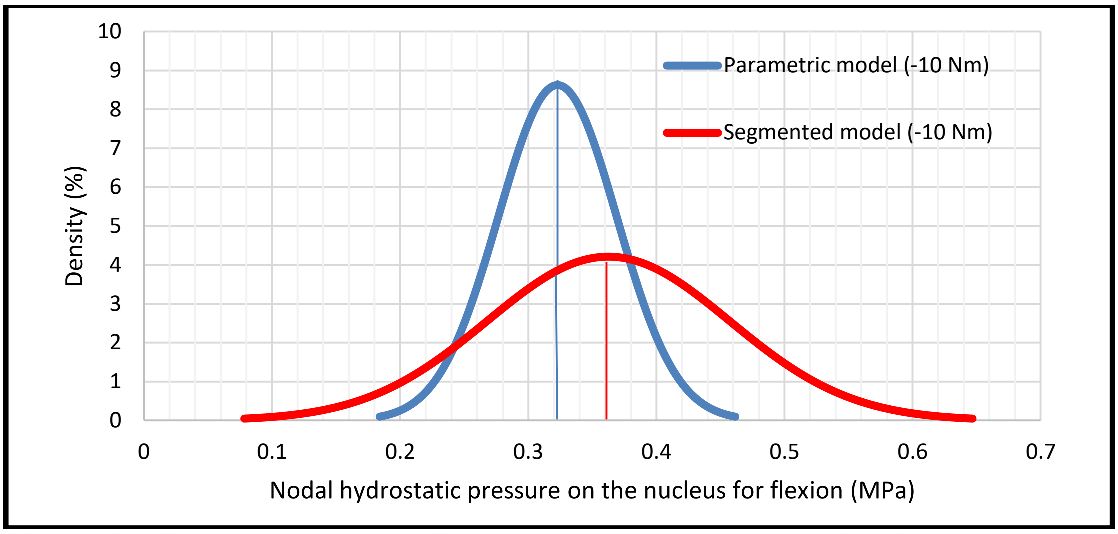

Figure 3.12. Nodal hydrostatic pressure density distribution in the nucleus from the FE models in flexion.

For extension, the mean value of the total nodal hydrostatic pressures was calculated as deneme –0.06 and –0.19 MPa for segmented and parametric FE models, respectively. Note that negative hydrostatic pressure values calculated for the extension since the nature of the extension motion is putting the nucleus under tension. The relative error of mean values between these FE models was 216 percent. Standard deviations were calculated as 0.30 MPa for the segmented, and 0.05 MPa for the parametric FE model. In summary, similar to flexion results, a wider variability on nodal hydrostatic pressure values was observed in the segmented FE model, and the variability between segmented and parametric FE models was more than that in flexion.

For lateral bending, the mean value of the total nodal hydrostatic pressures was calculated as 0.16 and 0.12 MPa for the segmented FE model results under 10Nm and –10 Nm pure moment loading, respectively. Note that the left and right rotations produced different angle responses due to the asymmetry of the segmented model geometry. The same quantity was calculated as 0.18 MPa for the parametric FE model in both directions. The relative error between the mean values of the segmented responses (left and right lateral bending) and the parametric response was 12 and 50 percent. Standard deviations were calculated as 0.51 MPa for both of the segmented FE model responses, and 0.43 MPa for the parametric FE model response. In summary, the total nodal hydrostatic pressure calculation of the FE models were observed to be in good agreement in lateral bending.

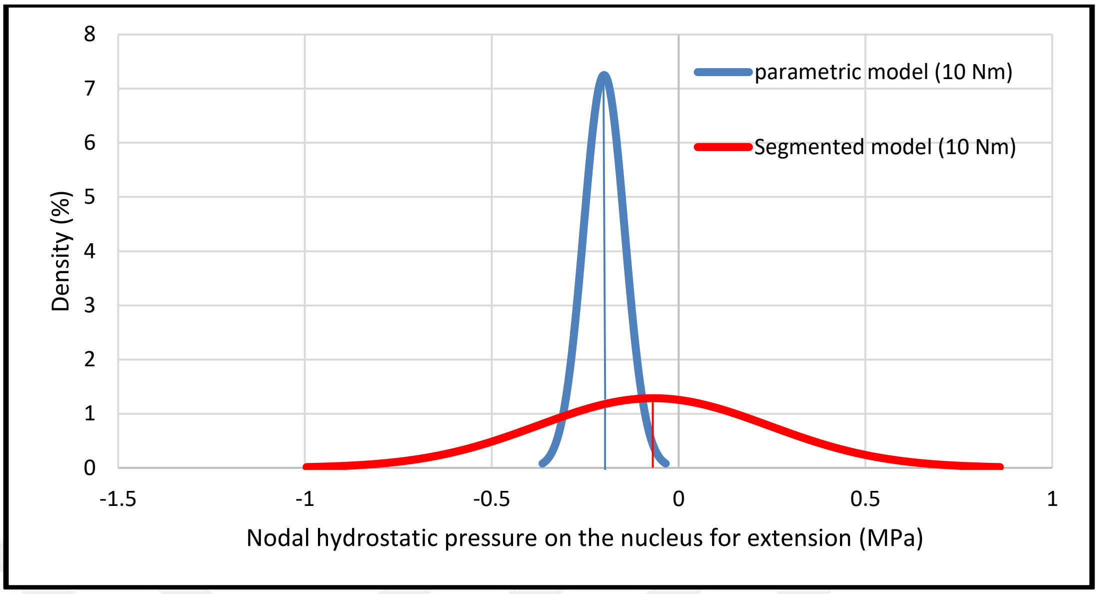

Figure 3.13. Nodal hydrostatic pressure density distribution in the nucleus from the FE models in extension.

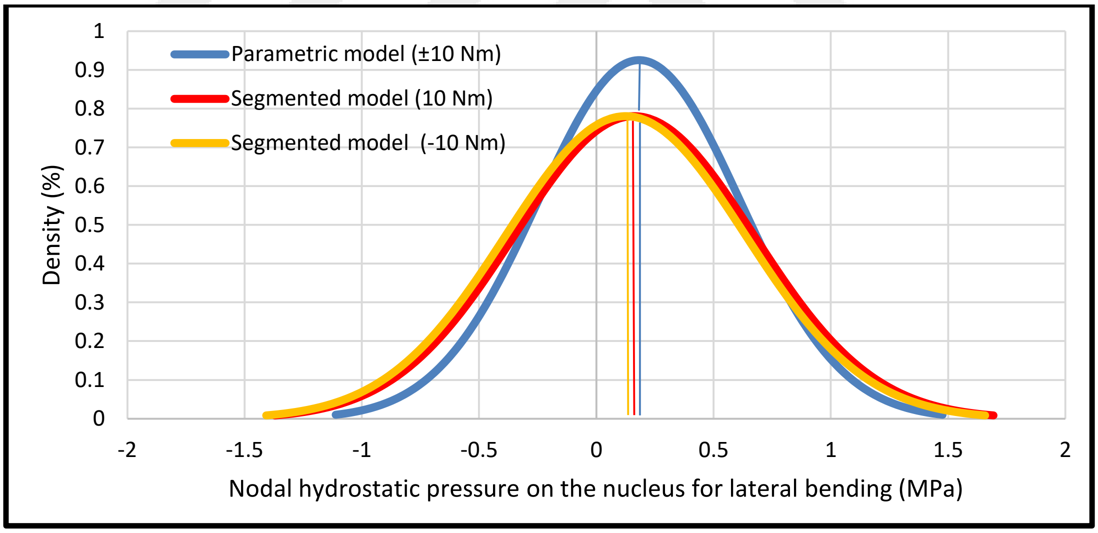

Figure 3.14. Nodal hydrostatic pressure density distribution in the nucleus from the FE models in lateral bending.

For axial rotation, the mean value of the total nodal hydrostatic pressures was calculated as 0.21 and 0.18 MPa for the segmented FE model results under 10Nm and –10 Nm pure moment loading, respectively. Note that the left and right rotations produced different angle responses due to the asymmetry of the segmented model geometry. The same quantity was calculated as 0.20 MPa for the parametric FE model in both directions. The relative error between the mean values of the segmented responses (left and right lateral bending) and the parametric response was 4 percent and 11 percent. Standard deviations were calculated as 0.20 MPa and 0.18 MPa for both of the segmented FE model responses, and 0.13 MPa for the parametric FE model response. In summary, the total nodal hydrostatic pressure calculation of the FE models were observed to be in good agreement in lateral bending.

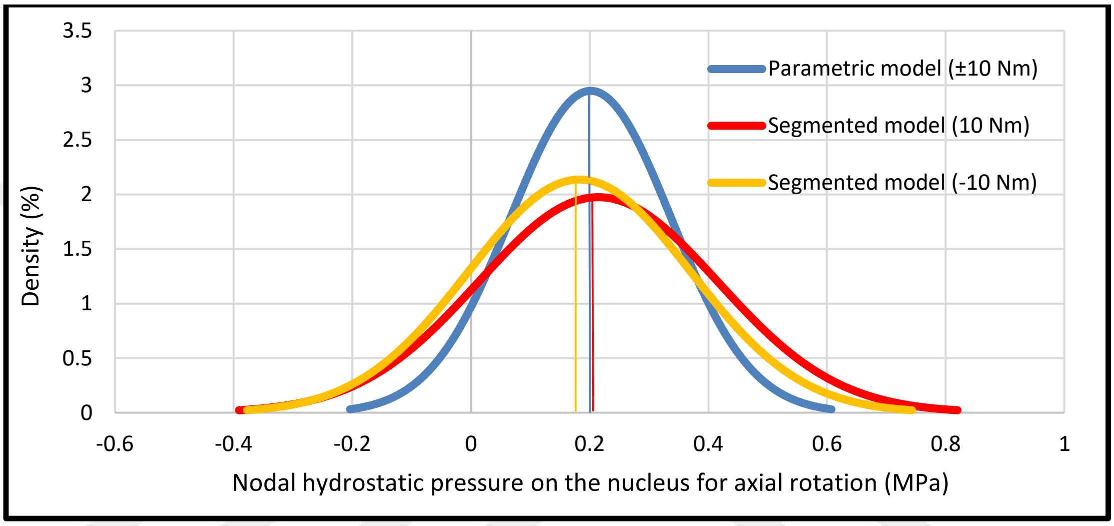

Figure 3.15. Nodal hydrostatic pressure density distribution in the nucleus from the FE models in axial rotation.

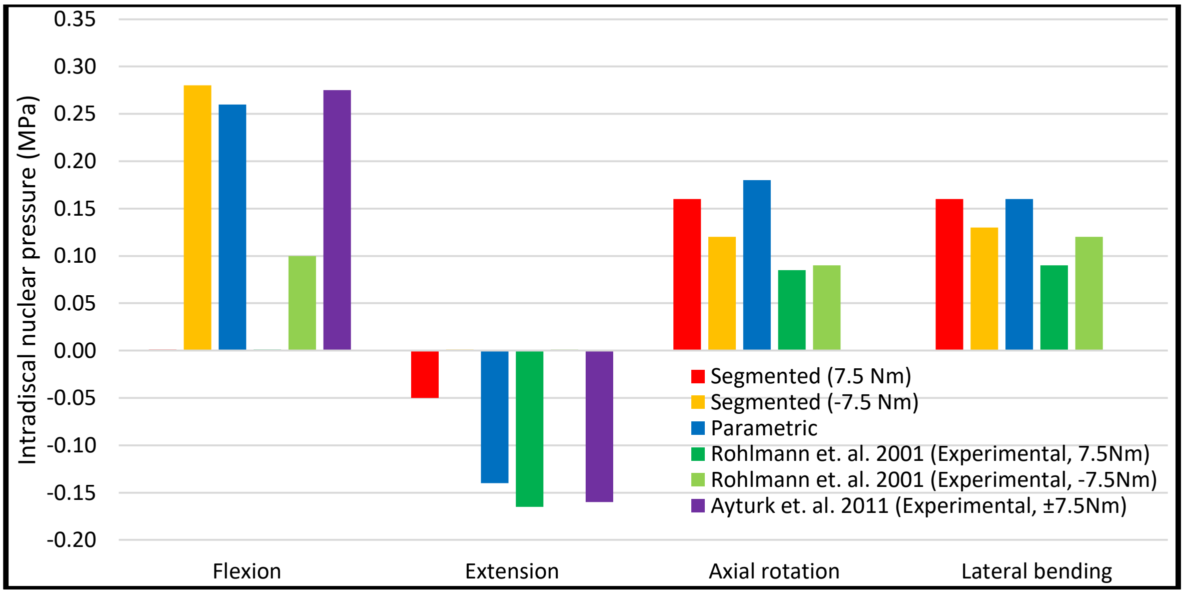

Figure 3.16. Comparison of IDP results from segmented and parametric FE models with the literature under 7.5 Nm pure-moment loading.

We compare our IDP results with the experimental and FE data provided by Ayturk et al. [30], and Rohlmann et al. [85], with a bar chart in Figure 3.16. In order to make this comparison, IDP data for 7.5 Nm pure-moment loading were collected from our model results similar to the studies of Ayturk et al. [30], and Rohlmann et al. [85].

When compared with the literature, flexion IDP results were observed to be in good agreement with the experimental data provided by Ayturk et al. [30]. However, the same was not observed with the experimental data of Rohlmann et al. [85]. Segmented and parametric FE model predictions of IDP for axial rotation and lateral bending were observed to be in a good agreement with the experimental data of Rohlmann et al. [85]. Data provided by Ayturk et al. [30] was only reporting the IDP results for flexion and extension. Therefore, we were only able to compare axial rotation and lateral bending results with Rohlmann et al. [85]. Under extension motion task, the IDP value from the parametric FE model was observed to be in good agreement with both of the experimental data presented here. However, the IDP values from the segmented FE model was observed to be less than experimental data. Overall, when segmented and parametric FE model results were compared with the literature, a good agreement with the experimental data was observed with the exception of extension motion task.

The mean value of the total nodal hydrostatic pressures for both segmented and parametric FE models during flexion/extension, lateral bending, and axial rotation are reported in Table 3.2.

Table 3.2. Mean of the total nodal hydrostatic pressure values for the segmented and parametric FE model under ±10 Nm pure moment load. “L” indicates a movement through the left lateral side, while “R” indicates the opposite, and “S” indicates the symmetry where the left and right results are the same.

	Mean value of the total nodal hydrostatic pressure (MPa)		
	Segmented		**Parametric**
Flexion (-10 Nm)	0.36		0.32
Extension (10 Nm)	-0.06		-0.19
Lateral bending (±10 Nm)	0.16 (L)	0.12 (R)	0.18 (S)
Axial rotation (±10 Nm)	0.21 (L)	0.18 (R)	0.20 (S)

3.2.3. Facet Joint Contact Force Response

FJFs of the segmented and the parametric FE models under ±7.5 Nm pure moment loading for the extension, lateral bending, and axial rotation were given together in Figure 3.17. In this figure, experimental data by Zhu et al. [86] and FE data validated by Schmidt et al. [87] were also included for validation. FJF data from the left and right facet joints were obtained separately from our FE models as well as those listed in the literature. Note that, for our parametric FE model and the FE model given by Schmidt et al. [87], FJF was provided for only one side due to their symmetry. The axial rotation and the lateral bending motions produced a non-zero FJF on the left side under a positive pure-moment loading, and on the right side under a negative pure-moment loading.

For the flexion, both of the segmented and parametric FE models provided 0 FJF force, since flexion motion is not causing contact between facet joints. Therefore, flexion FJF data was not presented in Figure 3.17.

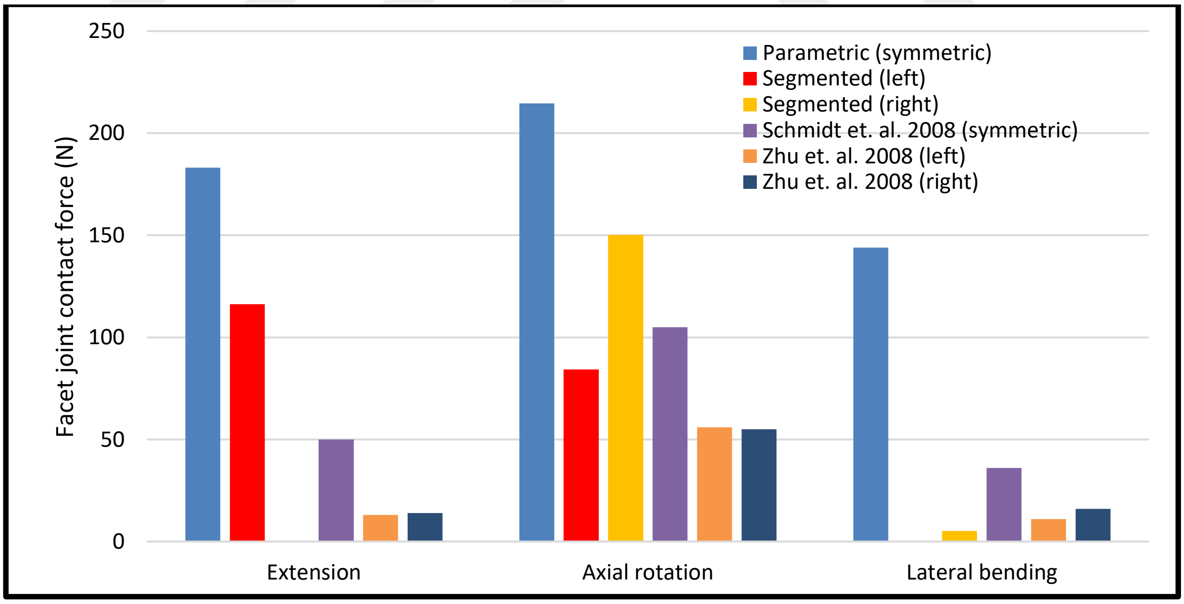

Figure 3.17. Comparison of FJF results of segmented and parametric FE models with the literature under 7.5 Nm pure-moment loading.

Due to the asymmetry of the segmented FE model geometry, contact was established only on the left lateral facet joint during extension motion. However,contact was established for both left and right lateral facet joints for the symmetric FE models (our parametric FE model and model by Schmidt et al. [87]). Similarly, the load was observed to be shared by left and right facet joints on the experimental data reported by Zhu et al. [86]. Therefore, it seemed more resonable to sum the FJF response from the left and right lateral facet joints, rather than comparing each side individually. In total, 159.18 N and 366.12 N FJF was calculated from both sides of the facet joints for the segmented and parametric FE model, respectively. The relative error between segmented and parametric FE model FJF results was 130 percent. Parametric FE model FJF results doubled the segmentation FE model results.

Compared with the literature, the total FJF values of the segmented FE model for extension was observed to be in good agreement with the FE data of Schmidt et al. [87]. However, the same agreement was not observed with the experimental data provided by Zhu et al. [86]. Parametric FE model results for the extension did not show an agreement with either experimental or FE data provided from the literature.

For axial rotation, 113.84 N and 203.87 N FJF were calculated for the segmented FE model. The same value was calculated as 214.57 N for the parametric FE model. The relative error between +10 Nm and -10 Nm loading condition results for the segmented FE model during axial rotation was 79 percent, whereas relative error between the average of left and right FJF values of the segmented FE model, and the FJF value (the left and right sides were not different as a result of symmetry) of the parametric FE model was 35 percent. For axial rotation direction of the applied pure moment was observed to be significantly affecting the FJFs, which was possible to observe through the difference between left and right lateral facet joint FJFs.

Compared with the literature, FJF values of the segmented FE model for axial rotation were in good agreement with the FE data of Schmidt et al. [87] but observed to be almost two times higher than the experimental data provided by Zhu et al. [86]. Parametric FE model results for the axial rotation did not show an agreement with either experimental or FE data provided from the literature, and even doubled the others.

For lateral bending, during the left lateral bending motion no contact between facet joints occured, whereas 6.39 N FJF was calculated for the right lateral bending motion of the segmented FE model. FJF was calculated as 143.95 N for the parametric FE model, which was observed as the lowest amongst all the other motion tasks. The lateral bending direction was observed to be significantly affecting the FJFs of the segmented FE model, reflected by the difference between left and right FJFs.

The FJFs of the segmented FE model in lateral bending were not in agreement with data from Schmidt et al. [87], but were more relatable with the experimental data provided by Zhu et al. [86]. Furthermore, parametric FE model results for lateral bending were not in agreement with either experimental or FE data, however, in general, the lateral bending FJF values turned out to be the lowest amongst all the other motion tasks, which agreed with the general trend.

Maximum FJF values for both segmented and parametric FE models during flexion/extension, lateral bending, and axial rotation are reported in Table 3.3.

Table 3.3. Maximum FJF responses of the segmented and parametric FE model under ±10 Nm pure moment load. . “L” indicates a movement through the left lateral side, while “R” indicates the opposite, and “S” indicates the symmetry where the left and right results are the same.

	Facet joint contact force (N)		
	Segmented		**Parametric**
Flexion (-10 Nm)	0.00		0.00
Extension (10 Nm)	159.18		183.06
Axial rotation (±10 Nm)	113.84 (L)	203.87 (R)	214.57 (S)
Lateral bending (±10 Nm)	0	6.39	143.95

4. DISCUSSION

In this study, two finite element (FE) models of the L4-5 spinal level were generated by using two distinct approach: segmentation developed using computed tomography (CT) scans of a patient, and a novel parametric CAD model that was fitted to the same patient’s CT scan.

Mesh density has been stated as an important indicator of the accuracy of an FE model [64]. In order to verify the level of accuracy, we performed two different mesh convergence studies for the intervertebral disc: (1) for the whole intervertebral disc, and (2) for the annulus fibrosus tissue only. In each approach, the mesh size was incrementally decreased by one half in each trial, starting from 5mm down to 0.15mm where possible. We compared the differences between every consecutive trial and determined the rate of reduction in error. In this way, a decreasing trend in relative error was observed, which pointed out the consistency of the numerical method.

As a second step, in order to validate the results of our numerical models, moment-rotation curves, Intradiscal nuclear pressure (IDP), and facet joint contact force (FJF) were chosen as validation metrics, and they were compared with data from the literature.

4.1. MODELING

The modeling and meshing process for the segmented model has proven to be time-consuming, as stated by many studies [17, 30]. It required a tedious segmentation, and an extensive geometrical clean-up process to make it ready for the meshing. On the other hand, the parametric computer-aided design (CAD) model was ready to mesh after updating it with the required morphometrical parameters. With respect to robustness and ease, parametric FE model development was superior to segmented FE model development in terms of time and effort required in the preparation phase.

Cortical bone, cancellous bone, and the posterior bony section of the vertebrae were generally modeled with linearly elastic and anisotropic material properties [47, 51, 88, 89]. There were also some reported studies that used linearly elastic and transversely isotropic materials for the cortical bone [30, 55]. For simplicity and robustness of the model meshing process, in this study, we chose the isotropic material model for the bony sections of the vertebra. Besides, the hexahedral meshing of the segmented model was nearly impossible with our current computational tools. However, the parametric CAD model used for this study provided us with the freedom of using hexahedral elements on the vertebral body. Hence, we also used hexahedral elements on the vertebral body. In order to accommodate the transverse isotropy of the bony sections in future models meshing was performed via hexahedral elements which allow for the material coordinate orientations to be specified. Even though the segmented FE model provided more geometrical detail, the parametric FE model was proved to be more superior to the segmented FE model in terms of meshability.

In order to avoid numerical instabilities that may occur due the highly non-linear features of the model including the contact interactions, geometric non-linearity, material non-linearity and incompressibility of soft tissues, hexahedral elements were preferred for the nucleus pulposis and the annulus fibrosus. Moreover, the use hexahedral elements in modeling the annulus fibrosus was essential due to its' anisotropic nature. The presence of the intervertebral disc (IVD) bulge made the semi-automatic modeling of the element coordinate system alignment almost impossible. Therefore IVD disc bulge was neglected.

The annulus fibrosus possesses concentric lamellae tissue that consist of collagen fiber tissue and non-fibrous matrix surrounding the nucleus pulposis. Collagen fibers of the AF are reported to be oriented at approximately 30 and 150 degrees with respect to the transverse plane of the spine [56]. The orientation angle of the collagen fibers was reported to be a function of circumferential position by Holzapfel et al. [58] and Coombs et al. [18]. Holzapfel et al. [58] reported that the orientation of collagen fibers also included a radial component. To date, an FE model study that implemented the radial fiber orientation has not been found in the literature. FE models of the lumbar spine throughout the literature were observed to be using either a single criss-cross angle throughout the annulus [shirazi] or four different angles for four angular regions (anterior, posterior, and left and right lateral section) of the annulus [18, 53]. Since our model was validated against the model described in Coombs et al. [18], we adopted the same approach in order to model the fibers of annulus fibrosus.

Modeling of the ligamentous tissue was an essential step since they provide the longest moment arms in the lumbar spine. Their influence on the mechanical behavior of the model was expected to be higher compared to other tissues. There were various approaches towards modeling of the ligamentous tissue of the lumbar spine. Rohlmann et al. [63] used one-dimensional elements to represent them and implemented their behavior by defining exponential force-displacement curves. These curves described the non-linear force-displacement behavior under tension. Another approach is to use regular truss elements in order to model the ligaments [47]. Finally, Coombs et al. [18] defined the linear spring-like behavior of the ligaments by using their mean stiffness values in tension. Even though this approach was more simplistic than the former ones, it captured a good fitting relation with experimental and FE results. In our study, we also used the mean parameters to define the stiffness of the ligaments similar to Coombs et al. [18]. We also observed that modeling the ligamentous tissue with mean stiffness parameters was satisfactory and practical.

4.2. MESH CONVERGENCE

Many previous authors stated that mesh density is an important parameter for verification directly related to the FE model predictions and solution accuracy [30, 53, 66]. In order to assess the convergence behavior, we performed a study based on systematically reducing the mesh (element) size [64]. Two different mesh convergence studies for the intervertebral disc were performed: (1) for the whole intervertebral disc, and (2) for the annulus tissue only. For each approach, mesh size was decreased by one half, starting from 5mm down to 0.15mm where possible.

For the convergence study of the IVD disc, a simplified geometry that was modeled with the IVD material properties was used. the relative error between the outputs of each consecutive mesh was calculated. Relative error calculations similar to this were also presented in the literature [30, 53]. As a result, we show that the displacement of nucleus pulposus (NP) and annulus fibrosus (AF) portrayed a convergence rate of O(h2). The relative error for the inest mesh (nucleus pulposus (NP) and annulus fibrosis (AP) for 0.8mm mesh size) was 1.3 percent for AF and 1.1 percent, respectively. For the NP the 0.8mm mesh size produced was also enough to observe convergence for the Cauchy stress calculations (0.4 percent). A convergence was not observed for the AF Cauchy stress value for this mesh size. Previously, Dreischarf et al. [31] compared the same validation metrics of eight different FE models of the lumbar spine. They reported that even though the models were different a good agreement between moment rotation curves was achieved. The IDP and FJF results didn’t match with each other nor they matched with the in vitro measurements. From this perspective our convergence results were in agreement with theirs. We confirmed that achieving convergence for the Cauchy stress is more challenging compared with displacements.

In order to further evaluate the Cauchy stress convergence of the AF, we performed another convergence study for the AF only. For this, analytical calculations of the thick-walled cylinder under internal pressure was used. A thick-walled cylinder FE model with the AF material properties was developed, and an inner pressure was applied. FE model Cauchy stress results in the inner radius was then compared with the analytical results, and relative error between them was calculated. Even though this approach was not representing the real boundary and loading conditions of AF, it allowed us to compare our FE model results with an analytical result. In this way, the convergence behavior of the AF material was observed. This convergence study was unique, and such a convergence study which compared the mesh refinement results with an analytical result in the FE model studies of the lumbar spine was not found in the previous literature. With this approach, we managed to refine our mesh even further and observed the convergence of Cauchy stress values. The mesh size that we started observing less than 10 percent error on Cauchy stress was 0.3mm which was approximately three times smaller than 0.8mm mesh size we used for this study. Due to limitations in the computational power, we continued with 0.8mm mesh size, which was more than enough for the convergence of displacement and Cauchy stress values of the nucleus, and the bone tissue of the vertebrae.

4.3. VALIDATION

In the literature, three main response parameters that were most frequently used in order to validate the FE models of the lumbar spine were the moment-rotation curves, the intradiscal nuclear pressures, and facet joint contact forces [31]. Therefore we also applied these parameters in validating our segmented and parametric FE models. Moment-rotation curves, IDPs, and FJFs were found on both the segmented and the parametric FE models results for different motion tasks, and were compared with the data from the literature.

The main goal behind many FE model studies of the lumbar spine is to simulate the *in vivo* behavior of the lumbar spine. In order to achieve that goal there are approaches such as applying a follower load and inclusion of spinal muscles [90–92]. However, even though such a model has the capability to represent reality better, boundary and loading conditions of the reality are still not that clear [93, 94]. Validating such a model is almost impossible since such an extensive *in vivo* database does not exist. Wilke et al. [95] managed to collect IDP data *in vivo* during various motion tasks, but, to the authors' knowledge, measuring many other valuable data is still not possible *in vivo* [64]. Therefore, in this study, we tried to mimic the *in vitro* experimental studies of the lumbar spine and performed our validation with the results of these studies. We tried to choose the simplest experimental studies to prevent any possible confusion about the boundary and the loading conditions. Furthermore, compared to *in vivo* data, there were many experimental studies in the literature that provided extensive *in vitro* data, which made the validation procedure easier.

Moment-rotation curve, IDP, and FJF of the segmented FE model were observed to be in good agreement with the literature, therefore they were successfully validated. Our results for the segmented FE model were between the range observed in the literature. The importance of the non-symmetric nature of the lumbar spine was significantly influencing the facet joint contact patterns, therefore, affecting the model predictions. This influence was mostly observed on the moment-rotation curve and FJF results of the extension, axial rotation, and lateral bending motion tasks. Initiation of the facet joint contact was causing an immediate increase in stiffness of the model.

The Moment-rotation curve and IDP values of the parametric FE model were also observed to be in good agreement with the literature with the exception of extension. FJF results of the parametric FE model were observed to be over predicted for all the motion tasks, which was almost double that of the results of the segmented FE model and the data from the literature. In general, extension results were behaving more stiffer than expected. This disagreement on the extension was caused by the early initiation of the contact interaction between the facet joints, as mentioned above. The main cause of this is thought to be the geometry of the facet joints. Overall, the parametric FE model was successful in capturing the moment-rotation curves and IDP values of the segmented FE model. However, it failed to capture the FJF results. Further study on the geometrical improvements of the facet joints and including the non-symmetry condition to the parametric CAD model was suggested in order to fully capture the biomechanical behavior.

Segmented FE model was observed to be providing reliable results, which would be quite beneficial on developing spinal implants, as well as patient-specific spinal implants and treatments. Furthermore, such a model would also be quite important for research purposes, since it allows researchers to measure data from locations where *in vitro/in vivo* data measurement is almost impossible. It could also be used to investigate spinal disorders or diseases with proper future work. Therefore, for detailed examination of the lumbar spine, development of segmented FE models are highly recommended.

Parametric FE models, on the other hand, prove its value over segmented FE models with its robustness and ease of FE model generation process. A trade-off was observed between the robust generation process and the accuracy of the results.

With the exception of extension, similar moment-rotation curve behaviors and IDP values were observed between the parametric and segmented FE models. That means the parametric model would be beneficial to quickly observe the effects of changes induced by factors such as implantations, on moment-rotation predictions, and IDP values. However, in order to understand the accuracy of the parametric FE model, the effects of the facet joint geometry on the moment-rotation curves and IDP also need to be evaluated in a future study.

As a design review decision, removal or serious reconsideration of the helical facet geometry is suggested in order to make the parametric FE model more physically realistic. Moreover, as a last remark, when considered as a part of a fully synthetic prosthesis, the geometry of the parametric vertebra CAD model could be utilized in order to transmit a larger portion of the load from the vertebral body to facet joints.

5. CONCLUSION

In this study, two FE models of the L4-5 spinal level was generated by using a segmentation model that was developed using CT scans of a patient, and a parametric model that was built with the same patient's measurements from the CT scan. In order to verify both of the models, mesh size was decided after an extensive mesh convergence study was performed. In order to validate them moment-rotation curves, IDP and FJF was chosen as validation metrics, and compared with the literature, as well as with each other.

Displacements of both models converged well after a couple of refinements. For isotropic media, convergence for both displacements and Cauchy stress was achieved. For anisotropic media, displacement convergence was achieved, but within our computational power limits, a reliable convergence for Cauchy stress was not observed. Relative error values calculated from our convergence studies were observed to be within 1.5 percent for displacements, and 1 percent for Cauchy stress of isotropic media, and within 24 percent for Cauchy stress of anisotropic media. Since annulus fibrosus was the only anisotropic media in the model, stresses in the annulus fibrosus were not used as a validation metric. However, for those who wish to read reliable stress data from the annulus fibrosus, further analysis would be necessary.

Moment-rotation curve, IDP, and FJF of the segmented FE model were observed to be in good agreement with the literature, therefore successfully validated. Significant variation in the data from the literature was observed, and our results were found to be within that range. The non-symmetric nature of the spine was observed to be heavily influencing the model predictions.

The moment-rotation curve of the parametric FE model was found to be in good agreement with the literature, with the exception of extension. Extension results were markedly more stiffer than expected. This disagreement on the extension was thought to be caused by the early start of the contact interaction between the facet joints. The main cause of this is thought to be the geometry of the facet joints. The early start of the contact interaction also showed its effects on FJF results of the motion tasks where facet contact prevails (extension, lateral bending, and axial rotation). In these motion tasks the parametric model behaved more stiffer compared with the segmented FE model and literature data.

IDP results of the parametric FE model were observed to be in good agreement with the literature, with the exception of extension. Further study on the geometry of the facet joints and including the non-symmetry condition to the parametric CAD model is suggested in order to fully capture the biomechanical behavior.

REFERENCES

1. Hoy D, March L, Brooks P. The global burden of low back pain: estimates from the Global Burden of Disease 2010 study. *Ann Rheum Dis.* 2014; 73: 968–974.

2. Sivasubramaniam V, Patel HC, Ozdemir BA. Trends in hospital admissions and surgical procedures for degenerative lumbar spine disease in England: a 15-year time-series study. *BMJ Open.* 2015; 5: e009011.

3. Panjabi MM. Clinical spinal instability and low back pain. *J Electromyogr Kinesiol.* 2003; 13: 371–379.

4. Trainor TJ, Wiesel SW. Epidemiology of back pain in the athlete. *Clin Sports Med.* 2002;21:93–103.

5. Roussouly P, Pinheiro-Franco JL. Biomechanical analysis of the spino-pelvic organization and adaptation in pathology. *Eur Spine J.* 2011;20:609–618.

6. Chaléat-Valayer E, Mac-Thiong J-M, Paquet J. Sagittal spino-pelvic alignment in chronic low back pain. *Eur Spine J*. 2011;20:634–640.

7. Barrey C, Jund J, Noseda O. Sagittal balance of the pelvis-spine complex and lumbar degenerative diseases. A comparative study about 85 cases. *Eur Spine J.* 2007;16:1459–1467.

8. Tüzün Ç, Yorulmaz İ, Cindaş A. Low back pain and posture. *Clin Rheumatol.* 1999;18:308–312.

9. Pope MH, Novotny JE. Spinal biomechanics. *J Biomech Eng.* 1993;115(4B):569-574

10. Sizer PS, Phelps V, Matthijs O. Pain generators of the lumbar spine. *Pain Pract.* 2001;1:255–273.

11. Hallab NJ, Singh V. Intervertebral disc joint replacement technology. *Joint Replacement Technology*. 2008:531–570.

12. Chow DHK, Luk KDK, Evans JH. Effects of short anterior lumbar interbody fusion on biomechanics of neighboring unfused segments. *Spine.* 1996;21:549–555.

13. Kumar M, Baklanov A, Chopin D. Correlation between sagittal plane changes and adjacent segment degeneration following lumbar spine fusion. *Eur Spine J.* 2001;10:314–319.

14. Naserkhaki S, Jaremko JL, El-Rich M. Effects of inter-individual lumbar spine geometry variation on load-sharing: geometrically personalized finite element study. *J Biomech.* 2016;49:2909–2917.

15. Aitchison G, Hukins DW, Parry J. A review of the design process for implantable orthopedic medical devices. *Open Biomed Eng J.* 2009;3:21–27.

16. Ransford B, Clark SS, Kune DF. Design challenges for secure implantable medical devices. *Security and Privacy for Implantable Medical Devices*. 2014:157–173.

17. Lavecchia CE, Espino DM, Moerman KM. Lumbar model generator: a tool for the automated generation of a parametric scalable model of the lumbar spine. *J R Soc Interface.* 2018;15:20170829.

18. Coombs DJ, Rullkoetter PJ, Laz PJ. Efficient probabilistic finite element analysis of a lumbar motion segment. *J Biomech.* 2017;61:65–74.

19. Chen S-H, Zhong Z-C, Chen C-S. Biomechanical comparison between lumbar disc arthroplasty and fusion. *Med Eng Phys.* 2009;31:244–253.

20. Hsu H-W, Zhong Z-C, Chen C-S. Effect of the cord pretension of the Dynesys dynamic stabilisation system on the biomechanics of the lumbar spine: a finite element analysis. *Eur Spine J.* 2011;20:1850–1858.

21. Putzer M, Ehrlich I, Rasmussen J. Sensitivity of lumbar spine loading to anatomical parameters. *J Biomech.* 2016;49:953–958.

22. Shirazi-Adl SA, Shrivastava SC, Ahmed AM. Stress analysis of the lumbar disc-body unit in compression. A three-dimensional nonlinear finite element study. *Spine.* 1984;9:120–134.

23. Lu YM, Hutton WC, Gharpuray VM. Can variations in intervertebral disc height affect the mechanical function of the disc? *Spine.* 1996; 21: 2208–2217.

24. Zander T, Rohlmann A, Calisse J. Estimation of muscle forces in the lumbar spine

during upper-body inclination. *Clin Biomech.* 2001;16:S73–S80.

25. Natarajan RN, Williams JR, Andersson GBJ. Modeling changes in Intervertebral Disc Mechanics with Degeneration. *J Bone Jt Surgery-American.* 2006;88:36–40.

26. Schmidt H, Heuer F, Simon U. Application of a new calibration method for a three-dimensional finite element model of a human lumbar annulus fibrosus. *Clin Biomech.* 2006;21:337–344.

27. Bruno AG, Anderson DE, D'Agostino J. The effect of thoracic kyphosis and sagittal plane alignment on vertebral compressive loading. *J Bone Miner Res.* 2012;27:2144–2151.

28. Arjmand N, Shirazi-Adl A. Biomechanics of hanges in lumbar posture in static lifting. *Spine.* 2005;30:2637–2648.

29. Shirazi-Adl A, Parnianpour M. Role of posture in mechanics of the lumbar spine in compression. *J Spinal Disord.* 1996;9:277–286.

30. Ayturk UM, Puttlitz CM. Parametric convergence sensitivity and validation of a finite element model of the human lumbar spine. *Comput Methods Biomech Biomed Engin.* 2011;14:695–705.

31. Dreischarf M, Zander T, Shirazi-Adl A. Comparison of eight published static finite element models of the intact lumbar spine: predictive power of models improves when combined together. *J Biomech.* 2014;47:1757–1766.

32. Whyne CM, Hu SS, Lotz JC. Parametric finite element analysis of verterbral bodies affected by tumors. *J Biomech.* 2001;34:1317–1324.

33. Grieve GP. Clinical anatomy of the lumbar spine and sacrum. *Physiotherapy.* 1997;83:495.

34. Goel VK, Monroe BT, Gilbertson LG. Interlaminar Shear Stresses and Laminae Separation in a Disc. *Spine.* 1995;20:689–698.

35. Liebschner MAK, Kopperdahl DL, Rosenberg WS. Finite element modeling of the human thoracolumbar spine. *Spine.* 2003;28:559–565.

36. Little JP, Pearcy MJ, Pettet GJ. Parametric equations to represent the profile of the human intervertebral disc in the transverse plane. *Med Biol Eng Comput.* 2007;45:939–945.

37. Kunkel ME, Schmidt H, Wilke H-J. Prediction equations for human thoracic and lumbar vertebral morphometry. *J Anat.* 2010;216:320–328.

38. Cappetti N, Naddeo A, Pellegrino A. Parametric model of lumbar vertebra. *J Ind Des Eng Graph.* 2010;5:15–18.

39. Lavaste F, Skalli W, Robin S. Three-dimensional geometrical and mechanical modelling of the lumbar spine. *J Biomech.* 1992;25:1153–1164.

40. Niemeyer F, Wilke H-JJ, Schmidt H. Geometry strongly influences the response of numerical models of the lumbar spine - a probabilistic finite element analysis. *J Biomech.* 2012;45:1414–1423.

41. Noailly J, Wilke H-J, Planell JA. How does the geometry affect the internal biomechanics of a lumbar spine bi-segment finite element model? Consequences on the validation process. *J Biomech.* 2007;40:2414–2425.

42. Biau DJ, Kernéis S, Porcher R. Statistics in Brief: the importance of sample size in the planning and interpretation of medical research. *Clin Orthop Relat Res.* 2008;466:2282–2288.

43. Shirazi-Adl A. Analysis of Role of Bone Compliance on Mechanics of a Lumbar Motion Segment. *J Biomech Eng.* 1994;116:408.

44. Okyar F, Guldeniz O, Atalay B. A holistic parametric design attempt towards geometric modeling of the lumbar spine. *Comput Methods Biomech Biomed Eng Imaging Vis.* 2019;1–11.

45. Breau C, Shirazi-Adl A, De Guise J. Reconstruction of a human ligamentous lumbar spine using CT images - a three-dimensional finite element mesh generation. *Ann Biomed Eng.* 1991;19:291–302.

46. Tyndyk MA, Barron V, McHugh PE, Mahoney DO. Generation of a finite element model of the thoracolumbar spine. *Acta Bioeng Biomech.* 2007;9:35–46.

47. Park WM, Kim K, Kim YH. Effects of degenerated intervertebral discs on intersegmental rotations, intradiscal pressures, and facet joint forces of the whole lumbar spine. *Comput Biol Med*. 2013;43:1234–1240.

48. Smit TH. The mechanical significance of the trabecular bone architecture in a human vertebra. 1996.

49. Wilke H-J, Bauer L, Bergmann G. Determination of trunk muscle forces for flexion and extension by using a validated finite element model of the lumbar spine and measured in vivo data. *J Biomech.* 2005;39:981–989.

50. Ezquerro F, Simón A, Prado M. Combination of finite element modeling and optimization for the study of lumbar spine biomechanics considering the 3D thorax-pelvis orientation. *Med Eng Phys.* 2004;26:11–22.

51. Little JP, De Visser H, Pearcy MJ. Are coupled rotations in the lumbar spine largely due to the osseo-ligamentous anatomy?—A modeling study. *Comput Methods Biomech Biomed Engin.* 2008;11:95–103.

52. Pellegrino A, Solitro GF, Naddeo A. Spinal FEM analyses based on parametric CAD model of vertebra. 2008.

53. Campbell JQ, Coombs DJ, Rao M. Automated finite element meshing of the lumbar spine: Verification and validation with 18 specimen-specific models. *J Biomech.* 2016;49:2669–2676.

54. White, AA, Panjabi M. *Clinical Biomechanics of the Spine*. 2nd ed. Philadelphia: Lippincott; 1990.

55. Schmidt H, Galbusera F, Rohlmann A. Effect of multilevel lumbar disc arthroplasty on spine kinematics and facet joint loads in flexion and extension: A finite element analysis. *Eur Spine J.* 2012;21(5):663-74.

56. Roberts S, Evans H, Trivedi J. Histology and pathology of the human intervertebral disc. *J Bone Jt Surg.* 2006;88:10–14.

57. Inoue H. Three-dimensional architecture of lumbar intervertebral discs. *Spine.* 1981;6:139–146.

58. Holzapfel GA, Schulze-Bauer CAJ, Feigl G. Single lamellar mechanics of the human lumbar anulus fibrosus. *Biomech Model Mechanobiol.* 2005;3:125–140.

59. Ghosh P, Bushell GR, Taylor TFK. Collagens, elastin and noncollagenous protein of the intervertebral disc. *Clin Orthop Relat Res.* 1977;129:124.

60. Shirazi-Adl A. Biomechanics of the lumbar spine in sagittal/lateral moments. *Spine.* 1994;19:2407–14.

61. Behrsin JF, Briggs CA. Ligaments of the lumbar spine: a review. *Surg Radiol Anat.* 1988;10:211–219.

62. Bridwell K, Ligaments. 2019 [cited 2020 17 May]. Available from: https://www.spineuniverse.com/anatomy/ligaments.

63. Rohlmann A, Mann A, Zander T. Effect of an artificial disc on lumbar spine biomechanics: a probabilistic finite element study. *Eur Spine J.* 2009;18:89–97.

64. Anderson AE, Ellis BJ, Weiss JA. Verification, validation and sensitivity studies in computational biomechanics. *Comput Methods Biomech Biomed Engin.* 2007;10:171–184.

65. Crawford RP, Rosenberg WS, Keaveny TM. Quantitative computed tomography-based finite element models of the human lumbar vertebral body: effect of element size on stiffness, damage, and fracture strength predictions. *J Biomech Eng.* 2003;125:434–438.

66. Jones AC, Wilcox RK. Finite element analysis of the spine: towards a framework of verification, validation and sensitivity analysis. *Med Eng Phys.* 2008;30:1287–1304.

67. Oberkampf WL, Trucano TG, Hirsch C. Verification, validation, and predictive capability in computational engineering and physics. *Appl Mech Rev.* 2004;57:345–384.

68. Roache PJ. *Verification and validation in computational science and engineering*. Albuquerque, NM: Hermosa; 1998.

69. AIAA Standards Committee. *AIAA Guide for the Verification and Validation of Computational Fluid Dynamics Simulations.* AIAA, Reston, VA, AIAA Standard No.

G-077-1998. 1998.

70. Blottner FG. Accurate Navier-Stokes results for the hypersonic flow over a spherical nosetip. *Journal of spacecraft and Rockets.* 1990;27(2):113-22.

71. Boehm BW. Software engineering economics. *IEEE Trans Softw Eng.* 1984;4-21.

72. Stern F, Wilson R V., Coleman HW. Comprehensive approach to verification and validation of CFD simulations - part 1: methodology and procedures. *J Fluids Eng.* 2001;123:793–802.

73. Einstein DR, Reinhall P, Nicosia M. Dynamic finite element implementation of nonlinear, anisotropic hyperelastic biological membranes. *Comput Methods Biomech. Biomed Engin.* 2003;6:33–44.

74. Weiss JA, Gardiner JC, Ellis BJ. Three-dimensional finite element modeling of ligaments: technical aspects. *Med Eng Phys.* 2005;27:845–861.

75. Ellis BJ, Debski RE, Moore SM. Methodology and sensitivity studies for finite element modeling of the inferior glenohumeral ligament complex. *J Biomech.* 2007;40:603–612.

76. Fedorov A, Beichel R, Kalpathy-Cramer J. 3D Slicer as an image computing platform for the Quantitative Imaging Network. *Magn Reson Imaging.* 2012;30:1323–1341.

77. Kikinis R, Pieper SD, Vosburgh KG. 3D Slicer: A platform for subject-specific image analysis, visualization, and clinical support. *Intraoperative Imaging and Image-Guided Therapy*. 2014:277–289.

78. 3D Systems, What Is An STL File? 2019 [cited 2020 17 May]. Available from: https://www.3dsystems.com/quickparts/learning-center/what-is-stl-file.

79. Guisheng Fang, Zengfang Li. Development of a sketching CAD system based on Parasolid. *9th International Conference on Computer-Aided Industrial Design and Conceptual Design on;* 2008:IEEE.

80. Den Hartog JP. *Advanced strength of materials*. New York: Dower Publications; 1987.

81. Guan Y, Yoganandan N, Zhang J. Validation of a clinical finite element model of the human lumbosacral spine. *Med Biol Eng Comput.* 2006;44:633–641.

82. Campbell J, Imsdahl S, Ching R. Evaluation of a synthetic L2-L5 spine model for biomechanical testing. 2012.

83. Rao M. Explicit finite element modeling of the lumbar spine. 2012.

84. Guan Y, Yoganandan N, Moore J. Moment–rotation responses of the human lumbosacral spinal column. *J Biomech.* 2007;40:1975–1980.

85. Rohlmann A, Neller S, Claes L. Influence of a follower load on intradiscal pressure and intersegmental rotation of the lumbar spine. *Spine.* 2001;26:557–561.

86. Zhu QA, Park YB, Sjovold SG. Can extra-articular strains be used to measure facet contact forces in the lumbar spine? An in-vitro biomechanical study. *Proc Inst Mech Eng Part H J Eng Med.* 2008;222:171–184.

87. Schmidt H, Heuer F, Claes L. The relation between the instantaneous center of rotation and facet joint forces – A finite element analysis. *Clin Biomech.* 2008;23:270–278.

88. Rohlmann A, Zander T, Schmidt H. Analysis of the influence of disc degeneration on the mechanical behaviour of a lumbar motion segment using the finite element method. *J Biomech.* 2006;39:2484–2490.

89. Goel VK, Kong W, Han JS. A Combined Finite Element and Optimization Investigation of Lumbar Spine Mechanics With and Without Muscles. *Spine.* 1993;18:1531–1541.

90. Kim YH. Role of trunk muscles in generating follower load in the lumbar spine of neutral standing posture. *J Biomech Eng.* 2008;130:041005.

91. Zhang H, Zhu W. The path to deliver the most realistic follower load for a lumbar spine in standing posture: a finite element study. *J Biomech Eng.* 2019;141:031010.

92. Khoddam-Khorasani P, Arjmand N, Shirazi-Adl A. Trunk hybrid passive–active musculoskeletal modeling to determine the detailed T12–S1 response under in vivo loads. *Ann Biomed Eng.* 2018;46:1830–1843.

93. Amiri S, Naserkhaki S, Parnianpour M. Modeling and validation of a detailed FE viscoelastic lumbar spine model for vehicle occupant dummies. *Comput Biol Med*. 2018;99:191–200.

94. Zander T, Rohlmann A, Bergmann G. Influence of different artificial disc kinematics on spine biomechanics. *Clin Biomech.* 2009;24:135–142.

95. Wilke H-J, Neef P, Hinz B. Intradiscal pressure together with anthropometric data – a data set for the validation of models. *Clin Biomech.* 2001;16:S111–S126.